Journal of Computational Physics **179,** 95–126 (2002)
doi:10.1006/jcph.2002.7044

Lattice Kinetic Schemes for Magnetohydrodynamics

Paul J. Dellar[1]

Department of Applied Mathematics and Theoretical Physics, University of Cambridge, Silver Street, Cambridge CB3 9EW, United Kingdom
E-mail: pdellar@na-net.ornl.gov

Received May 21, 2001; revised January 11, 2002

Lattice kinetic equations for simulating incompressible magnetohydrodynamics in two or three dimensions are constructed. The fluid is simulated via a conventional low Mach number lattice Boltzmann scheme, modified to include the Lorentz force due to the magnetic field. The magnetic field is represented by a separate vector-valued magnetic distribution function which obeys a vector Boltzmann–BGK equation. The two distribution functions are only coupled via the macroscopic density, momentum, and magnetic field evaluated at lattice points. This allows a reduced lattice to be used for the magnetic distribution function, with a corresponding saving in storage, which becomes comparable to that for the scalar hydrodynamic distribution function. The magnetic diffusivity may be adjusted independently of the fluid viscosity, unlike an earlier formulation. Numerical experiments with Hartmann flow, the Orszag–Tang vortex, and the doubly periodic coalescence instability compare favorably with results obtained using a spectral method, and with previously published results. The scheme preserved a consistent approximation to the divergence-free condition $\nabla \cdot \mathbf{B} = 0$ to round-off error. © 2002 Elsevier Science (USA)

1. INTRODUCTION

Methods based on lattice Boltzmann equations (LBE) are a promising alternative to conventional numerical methods for simulating fluid flows [17, 38]. Using a velocity-space truncation of the Boltzmann equation (2) from the kinetic theory of gases [11, 12, 32, 40], lattice Boltzmann methods lead to linear, constant coefficient hyperbolic systems with nonlinear source terms. Such systems are straightforward to implement numerically and have proved especially effective for simulating flows in complicated geometries, and for exploiting massively parallel computer architectures. However, there have been very few

[1] Current address: OCIAM, Mathematical Institute, 24-29 St Giles', Oxford, OX1 3LB, UK.

0021-9991/02 $35.00
© 2002 Elsevier Science (USA)
All rights reserved.

previous applications to magnetohydrodynamics (MHD) [16, 54, 69]. Our approach is based upon work by Bouchut [7] that introduced a vector-valued distribution function in place of the scalar probability distribution function used in the kinetic theory of gases. At this point the connection with the Boltzmann equation becomes rather tenuous, so we propose the description "lattice kinetic scheme."

The two-dimensional incompressible "reduced" magnetohydrodynamic equations suffice to describe many processes occurring in three-dimensional compressible magnetised plasmas [4, 27, 50, 51]. Experiments in plasma physics are often conducted in a toroidal geometry, with the magnetic field predominantly in the azimuthal direction. A two-dimensional approximation may be justified on the assumption that the fields are slowly varying functions of the azimuthal coordinate, z say, so that $\partial_z \ll \partial_x, \partial_y$. The magnetic pressure due to the field component in the toroidal direction is often large enough, $B_z \gg B_x, B_y$, to justify an incompressibility approximation in the perpendicular xy-plane. A similar geometrical argument may be used to justify the reduced MHD equations in studies of solar coronal heating [27, 51]. We construct a numerical scheme based on kinetic theory that simulates the two- or three-dimensional compressible magnetohydrodynamic (MHD) equations at small but finite Mach numbers, for which solutions approximate solutions of the incompressible MHD equations.

The lattice Boltzmann approach to hydrodynamics leads to intrinsically multidimensional numerical schemes through the use of multidimensional lattices and quadratures to maintain isotropy of the derived equations. By contrast, the extension to multiple dimensions of conventional upwind schemes originally developed in one spatial dimension typically requires additional work [31, 46, 47]. This problem is particularly acute in magnetohydrodynamics owing to the constraint $\nabla \cdot \mathbf{B} = 0$. This expresses the absence of magnetic monopoles, which have never been observed experimentally. Since the magnetic induction equation (5) implies $\partial_t \nabla \cdot \mathbf{B} = 0$, this constraint is often imposed as an initial condition, one that is preserved by the evolution of $\mathbf{B}$. Unfortunately, this constraint makes the one-dimensional situation degenerate [48, 63]. If $\mathbf{B}$ is a function of one coordinate x only, then the constraint $\nabla \cdot \mathbf{B} = 0$ simplifies to $\partial_x B_x = 0$, forcing the x-component B_x of the magnetic field to be constant. Thus the solution of the compressible MHD Riemann problem contains only seven waves for a system of eight variables, so a separate step is normally required to evolve the B_x component [9, 73]. Conversely, if a multidimensional MHD system is solved by dimensional splitting, or even just uses one-dimensional Riemann problems to compute upwind fluxes, the initial data for these one-dimensional problems will generally not satisfy $\nabla \cdot \mathbf{B} = 0$ [63]. Numerous variants of these two approaches were compared recently by Tóth [71]. Our scheme avoids all these considerations by being genuinely multidimensional and preserves a consistent discrete approximation to $\nabla \cdot \mathbf{B} = 0$ to machine round-off error.

Kinetic formulations of the Euler or Navier–Stokes equations introduce a distribution function $f(\mathbf{x}, \boldsymbol{\xi}, t)$ that denotes the density of particles at position $\mathbf{x}$ and time t moving with microscopic velocity $\boldsymbol{\xi}$ [11, 12, 32, 40]. The macroscopic quantities such as density, ρ, momentum, $\rho\mathbf{u}$, and momentum flux or stress, $\boldsymbol{\Pi}$ [45], each of which depends on $\mathbf{x}$ and t only, are obtained from moments of the distribution function with respect to the microscopic velocity, $\boldsymbol{\xi}$,

$$\rho = \int f(\mathbf{x}, \boldsymbol{\xi}, t)\, d\boldsymbol{\xi}, \quad \rho\mathbf{u} = \int \boldsymbol{\xi} f(\mathbf{x}, \boldsymbol{\xi}, t)\, d\boldsymbol{\xi}, \quad \boldsymbol{\Pi} = \int \boldsymbol{\xi}\boldsymbol{\xi} f(\mathbf{x}, \boldsymbol{\xi}, t)\, d\boldsymbol{\xi}, \tag{1}$$

where the integrals are taken over all of velocity space. In the absence of external forces, such as gravity, the distribution function f evolves according to the Boltzmann equation

$$\partial_t f + \boldsymbol{\xi} \cdot \nabla f = C(f), \tag{2}$$

where the term $C(f)$ describes collisions between particles. Much of the computational interest in kinetic formulations is due to the linearity of the differential operator on the left hand side of (2). Nonlinearity is confined to the collision term, which is generally both nonlinear and nonlocal in that it involves integrals with respect to $\boldsymbol{\xi}$. The Bhatnagar–Gross–Krook (BGK) approximation [3] is often used for the collision term, in which f relaxes towards an equilibrium distribution $f^{(0)}$ with a single relaxation time τ,

$$\partial_t f + \boldsymbol{\xi} \cdot \nabla f = -\frac{1}{\tau}\left(f - f^{(0)}\right). \tag{3}$$

This approximation is sufficient to recover the Navier–Stokes equations, although with the limitation that the thermal conductivity κ is given by $\kappa = (5/2)\nu$, rather than $\kappa = (15/4)\nu$, as obtained from Boltzmann's binary collision operator [11].

By integrating (2) over $\boldsymbol{\xi}$, and by multiplying (2) by $\boldsymbol{\xi}$ and integrating, Eq. (2) implies macroscopic mass and momentum conservation equations in the form

$$\partial_t \rho + \nabla \cdot (\rho \mathbf{u}) = 0, \quad \partial_t (\rho \mathbf{u}) + \nabla \cdot \boldsymbol{\Pi} = 0. \tag{4}$$

The right hand sides, which are the zeroth and first moments of the collision term, $\int C(f)\, d\boldsymbol{\xi}$ and $\int \boldsymbol{\xi} C(f)\, d\boldsymbol{\xi}$, respectively, vanish because collisions between particles conserve mass and momentum. Although these continuum equations lack significant content until we can express the momentum flux, $\boldsymbol{\Pi}$, in terms of the macroscopic variables, their structure shows that the time derivative of momentum, which is a vector quantity, must be the divergence of a *symmetric* rank-2 tensor, since $\boldsymbol{\Pi}$ is symmetric by construction in (1). In heuristic constructions of continuum mechanics the symmetry of the stress tensor is a consequence of local angular momentum conservation, since any asymmetry of $\boldsymbol{\Pi}$ would induce arbitrarily large angular accelerations of small material volumes [45].

Conversely, the time evolution of a magnetic field $\mathbf{B}$ is determined by the associated electric field $\mathbf{E}$ through the induction equation [4, 67]

$$\frac{\partial \mathbf{B}}{\partial t} + \nabla \times \mathbf{E} = 0, \tag{5}$$

which is one of Maxwell's equations. This may be rewritten in a divergence form resembling (4),

$$\frac{\partial \mathbf{B}}{\partial t} + \nabla \cdot \boldsymbol{\Lambda} = 0, \tag{6}$$

if the electric field is represented as an *antisymmetric* rank-2 tensor $\boldsymbol{\Lambda}$ with components

$$\Lambda_{\alpha\beta} = -\epsilon_{\alpha\beta\gamma} E_\gamma, \tag{7}$$

where $\epsilon_{\alpha\beta\gamma}$ is the alternating Levi–Civita tensor. We follow Chen and Doolen [17] in using Greek indices for vector components, reserving Roman indices for labelling discrete lattice vectors.

Comparing (6) with (4), the asymmetry, in fact *antisymmetry*, of $\mathbf{\Lambda}$ makes it impossible to construct a kinetic formulation for the induction equation analogous to that for the Navier–Stokes momentum equation, in which the macroscopic magnetic field is the first moment of some scalar distribution function. Instead, following Croisille *et al*. [21] and Bouchut [7], we introduce a *vector-valued* distribution $\mathbf{g}(\mathbf{x}, \boldsymbol{\xi}, t)$ for the magnetic field such that

$$\mathbf{B}(\mathbf{x}, t) = \int \mathbf{g}(\mathbf{x}, \boldsymbol{\xi}, t)\, d\boldsymbol{\xi}. \tag{8}$$

We propose that $\mathbf{g}(\mathbf{x}, \boldsymbol{\xi}, t)$ should satisfy a vector Boltzmann–BGK equation of the kind considered by Bouchut [7],

$$\partial_t \mathbf{g} + \boldsymbol{\xi} \cdot \nabla \mathbf{g} = -\frac{1}{\tau_\mathrm{m}} \left(\mathbf{g} - \mathbf{g}^{(0)} \right), \tag{9}$$

so that each component of $\mathbf{g}$ satisfies an equation of the form (3). The use of a separate relaxation time $\tau_\mathrm{m} \neq \tau$ will allow the resistivity, the inverse of the electrical conductivity, to be adjusted independently of the fluid viscosity determined by τ.

Bouchut's goal was to construct continuum kinetic formulations for arbitrary systems of hyperbolic conservation laws satisfying certain entropy properties by introducing a distribution function with one component for each conserved variable in the original hyperbolic system [7]. More generally, Jin and Xin [44] proposed a scheme for solving nonlinear systems of hyperbolic conservation laws by embedding them in a larger *linear* hyperbolic system of the form (9) with an entropy-respecting relaxation term on the right hand side. The resulting linear system may be solved readily using a conventional upwind scheme [31, 46, 48]. This approach, based on theoretical work by Chen *et al*. [13], was recently reinterpreted by LeVeque and Pelanti [49] as defining a class of approximate Riemann solvers for the original hyperbolic system. However, in this paper we are a little more ambitious. Entropy-respecting hyperbolic schemes aim at best to capture the correct limiting solution of some hyperbolic system, as the diffusion coefficients tend to zero [31, 46]. By contrast, we show below that our lattice kinetic scheme captures the correct viscous and resistive transport behavior for finite values of the diffusion coefficients ν and η.

A vector-valued distribution function was used by Croisille *et al*. [21] in their "semiempirical" kinetic formulation of the ideal ($\eta = \nu = 0$) MHD equations. They used the alternative BGK-like evolution equation

$$\partial_t \mathbf{g} - \nabla \times (\boldsymbol{\xi} \times \mathbf{g}) = -\frac{1}{\tau_\mathrm{m}} \left(\mathbf{g} - \mathbf{g}^{(0)} \right) \tag{10}$$

to construct upwind fluxes as part of a finite-volume method for solving the compressible ideal MHD equations. The explicit curl in (10) is helpful for enforcing the divergence-free constraint $\nabla \cdot \mathbf{B} = 0$. Unfortunately it is not possible to solve (10) by integrating ordinary differential equations along characteristics, since the three components of $\mathbf{g}$ are coupled via the $\boldsymbol{\xi} \nabla \cdot \mathbf{g}$ term in $\nabla \times (\boldsymbol{\xi} \times \mathbf{g}) = \boldsymbol{\xi} \cdot \nabla \mathbf{g} - \boldsymbol{\xi} \nabla \cdot \mathbf{g}$, so it is not suitable for a lattice Boltzmann method (see Section 7).

While lattice Boltzmann equations were originally constructed empirically [55] as extensions of lattice gas automata (LGA) [30] to continuous distribution functions, it was eventually realised that the most common isothermal LBE is equivalent to a systematic moment truncation of the continuum Boltzmann equation in velocity space [35, 36, 66]. This

approach is useful for ensuring that the LBE reproduces the correct continuum behavior, but it suffers from the drawback that constraints on the moments of the distribution functions appearing in the continuum equations generally do not suffice to determine a unique set of equilibria [23]. In particular, the fact that a proposed LBE reproduces the desired continuum behavior for slowly varying solutions does not prevent it from being unstable to grid-scale instabilities [23].

Chen *et al*. [16] proposed a lattice Boltzmann scheme for MHD using a set of distribution functions f_{ij} with two suffixes, corresponding to separate microscopic velocities for $\mathbf{u}$ and $\mathbf{B}$. The macroscopic velocity and magnetic fields were reconstructed from moments with respect to i and j, respectively. This formulation arose as a continuum generalisation of the stochastic bidirectional streaming previously employed in lattice gas MHD cellular automata [15, 18]. However, such a large collection of distribution functions requires an unreasonably large number of variables per lattice point, namely 36 for the minimal two-dimensional hexagonal lattice, and several hundred for a three-dimensional implementation. Martínez *et al*. [54] reduced the number of variables to only twice that required for a Navier–Stokes simulation by using a sparse set of distribution functions with f_{ij} identically zero for most combinations of i and j, but did not address the more serious drawback that the use of a single set of distribution functions for both $\mathbf{B}$ and $\mathbf{u}$ implies a fixed algebraic relation between the viscosity ν and resistivity η. In particular, they were unable to achieve high fluid Reynolds numbers with their scheme.

Another approach for two-dimensional MHD [57, 69] uses the magnetic vector potential, or flux function, formulation (see Section 9). Succi *et al*. [69] observed that in the incompressible Navier–Stokes equation for a three-dimensional velocity field which is a function of only two coordinates, such as $(u_x, u_y, u_z)(x, y)$, the third velocity component u_z is advected like a passive scalar. Thus they could simulate two-dimensional MHD by identifying u_z with a magnetic flux function (see Section 9), and modifying the equilibrium distribution to include the Lorentz force. However this approach does not extend into three dimensions and is also limited by the requirement that the viscosity ν and resistivity η be equal.

2. MAGNETOHYDRODYNAMIC EQUATIONS

The incompressible magnetohydrodynamic (MHD) equations are [4, 67]

$$\partial_t \mathbf{u} + \mathbf{u} \cdot \nabla \mathbf{u} = -\rho_0^{-1} \nabla p + \rho_0^{-1} \mathbf{J} \times \mathbf{B} + \nu \nabla^2 \mathbf{u}, \tag{11a}$$

$$\partial_t \mathbf{B} = -\nabla \times \mathbf{E} = \nabla \times (\mathbf{u} \times \mathbf{B} - \eta \nabla \times \mathbf{B}), \tag{11b}$$

subject to the two divergence-free constraints $\nabla \cdot \mathbf{u} = 0$ and $\nabla \cdot \mathbf{B} = 0$. The electric field $\mathbf{E}$ has been eliminated using Ohm's law in the usual resistive MHD approximation, $\mathbf{E} + \mathbf{u} \times \mathbf{B} = \eta \nabla \times \mathbf{B}$ [4, 67]. The magnetic permittivity μ_0 has been absorbed by replacing $\mathbf{B}$ with $\mathbf{B}\mu_0^{-1/2}$, but a reference density, ρ_0, has been retained to aid comparison with the compressible magnetohydrodynamic equations appearing below. Thus some of our formulae, notably those for Hartmann flow in Section 8, differ from those of Martínez *et al*. [54], who replaced $\mathbf{B}$ with the Alfvén velocity $\mathbf{B}/(\rho_0\mu_0)^{1/2}$ to absorb the ρ_0^{-1} term in front of $\mathbf{J} \times \mathbf{B}$ in (11a) as well. The two diffusion coefficients ν and η are the kinematic viscosity and magnetic resistivity, respectively. The relative importance of the viscous and resistive terms in the momentum and induction equations, respectively, is denoted by two

dimensionless parameters, the Reynolds number $\mathrm{Re} = UL/\nu$ and the magnetic Reynolds number $\mathrm{Rm} = UL/\eta$, where U and L are velocity and length scales.

The divergence-free condition in the magnetic induction equation (11b) differs in character to that in the Navier–Stokes equation (11a). Since the divergence of the right hand side $-\nabla \times \mathbf{E}$ vanishes identically, $\partial_t \nabla \cdot \mathbf{B} = 0$. The constraint $\nabla \cdot \mathbf{B} = 0$ may thus be thought of as an initial condition, one that is preserved by the evolution equation (11b). By contrast, the divergence-free condition $\nabla \cdot \mathbf{u} = 0$ must be explicitly enforced by the pressure gradient in the Navier–Stokes equation (11a), since the nonlinear terms $\mathbf{u} \cdot \nabla \mathbf{u}$ and $\mathbf{J} \times \mathbf{B}$ generally have nonzero divergence. We show in Section 6 that our scheme preserves a consistent approximation to $\nabla \cdot \mathbf{B} = 0$.

We actually simulate the compressible Navier–Stokes equations, in which the nonlocal Poisson equation for the pressure, obtained by taking the divergence of equation (11a), is replaced by the local propagation of sound waves at a finite speed, c_s. Solutions of the compressible system approximate solutions of the incompressible system when the sound speed c_s is much larger than the fluid speed $\mathbf{u}$, which is the limit of small Mach number, $\mathrm{Ma} = |\mathbf{u}|/c_\mathrm{s} \to 0$. Thus we replace the incompressible MHD system (11a) and (11b) with the compressible system

$$\partial_t \rho + \nabla \cdot (\rho \mathbf{u}) = 0, \tag{12a}$$

$$\partial_t (\rho \mathbf{u}) + \nabla \cdot (p \mathsf{I} + \rho \mathbf{u}\mathbf{u}) = \mathbf{J} \times \mathbf{B} + \nabla \cdot (2\nu\rho \mathsf{S}), \tag{12b}$$

$$\partial_t \mathbf{B} + \nabla \cdot (\mathbf{u}\mathbf{B} - \mathbf{B}\mathbf{u}) = \eta \nabla^2 \mathbf{B}. \tag{12c}$$

The viscous stress has been written as a scalar multiple of the strain tensor $S_{\alpha\beta} = \frac{1}{2}(\partial_\alpha u_\beta + \partial_\beta u_\alpha)$. This differs from the usual compressible Navier–Stokes viscous stress because the strain tensor is not traceless, so the simulated fluid possesses bulk viscosity as well as shear viscosity. However, this is the form that emerges from an isothermal lattice Boltzmann equation (see [25] and (25) below), and the missing isotropic term proportional to $\nabla \cdot \mathbf{u}$ becomes negligible compared with the other terms in the small Mach number limit. Similarly, the resistive term $-\nabla \times (\eta \nabla \times \mathbf{B})$ has been rewritten as $\eta \nabla^2 \mathbf{B}$ in (12b), using the assumptions that η is constant and that $\nabla \cdot \mathbf{B} = 0$.

We construct lattice kinetic equations that simulate the system (12a)–(12c) in the small Mach number limit. For scaling purposes, we assume that the two nonlinear terms $\rho \mathbf{u}^2$ and $\mathbf{B}^2$ are comparable (see Section 4), or in other words that the fluid velocity $\mathbf{u}$ is comparable with the Alfvén velocity $\mathbf{u}_\mathrm{A} = \mathbf{B}\rho^{-1/2}$ (recall that we have absorbed a factor of $\mu_0^{-1/2}$ into $\mathbf{B}$). In the small Mach number limit, temperature and density variations are both $O(\mathrm{Ma}^2)$. It is thus common to adopt the isothermal equation of state $p = c_\mathrm{s}^2 \rho$, with constant sound speed c_s, when devising lattice Boltzmann equations [17, 64]. We adopt scalings in which the density and sound speed c_s are $O(1)$, and the fluid velocity and magnetic field are both $O(\mathrm{Ma})$. The small Mach number limit allows the neglect of various small terms associated with higher moments of the two distribution functions f and $\mathbf{g}$. In other words, f and $\mathbf{g}$ may be accurately represented by their first few moments with respect to the microscopic velocity $\boldsymbol{\xi}$.

3. HYDRODYNAMIC LATTICE BOLTZMANN EQUATION

Conventional lattice Boltzmann equations simulate the isothermal compressible Navier–Stokes equations, with no magnetic field, in the limit of small mean free path [17, 64]. The

macroscopic quantities of density ρ, momentum $\rho\mathbf{u}$, and stress $\mathbf{\Pi}$ are given by moments of a set of N scalar distribution functions $f_i(\mathbf{x}, t)$, where $i = 1, \ldots, N$,

$$\rho = \sum_{i=0}^{N} f_i, \quad \rho\mathbf{u} = \sum_{i=0}^{N} \boldsymbol{\xi}_i f_i, \quad \mathbf{\Pi} = \sum_{i=0}^{N} \boldsymbol{\xi}_i \boldsymbol{\xi}_i f_i, \tag{13}$$

which is the discrete analogue of the integral moments in (1). The derivation is very similar to the classical derivation of the Navier–Stokes equations from the continuum Boltzmann equation [11, 12, 32, 40], except that integrals with respect to $\boldsymbol{\xi}$ are replaced by sums over $\boldsymbol{\xi}_i$.

Each vector $\boldsymbol{\xi}_i$ may be thought of as a particle speed associated with a distribution function f_i. As explained below, the set of velocity vectors $\boldsymbol{\xi}_i$ fit together to form a lattice in velocity space, which becomes a lattice in physical space when the equations are integrated over a time interval Δt. Alternatively, the $\boldsymbol{\xi}_i$ may be thought of as nodes in a Gaussian quadrature formula for the moments with respect to $\boldsymbol{\xi}$ of a distribution function $f(\mathbf{x}, t, \boldsymbol{\xi})$ that varies continuously with $\boldsymbol{\xi}$, in which case the particular hydrodynamic lattice Boltzmann equation below corresponds to a systematic truncation of the continuum Boltzmann equation in velocity space [24, 35, 36, 66].

The distribution functions f_i evolve according to the lattice Boltzmann equation,

$$\partial_t f_i + \boldsymbol{\xi}_i \cdot \nabla f_i = -\frac{1}{\epsilon\tau}\left(f_i - f_i^{(0)}\right), \quad \text{for } i = 0, \ldots, N. \tag{14}$$

Again, the right hand side uses the BGK approximation [3] to the collision term, as in (3). The small parameter ϵ has been introduced so that solutions to (14) may be constructed via a multiple scales expansion in ϵ. The parameter ϵ may be identified physically with the dimensionless mean free path, or Knudsen number, or with a computational grid spacing, but its main purpose is to avoid the moment closure problem that plagues hydrodynamic turbulence [4, 45].

The Chapman–Enskog expansion poses a multiple scale expansion of both f and t, but not $\mathbf{x}$, in powers of the small parameter ϵ,

$$f_i = f_i^{(0)} + \epsilon f_i^{(1)} + \epsilon^2 f_i^{(2)} + \cdots, \quad \partial_t = \partial_{t_0} + \epsilon\partial_{t_1} + \cdots, \tag{15}$$

where t_0 and t_1 are advective and diffusive timescales, respectively. We impose the solvability conditions

$$\sum_{i=0}^{N} f_i^{(n)} = 0, \quad \sum_{i=0}^{N} \boldsymbol{\xi}_i f_i^{(n)} = 0, \quad \text{for } n = 1, 2, \ldots, \tag{16}$$

so the higher order terms $f_i^{(1)}, f_i^{(2)}, \ldots$, do not contribute to the macroscopic density or momentum. These constraints imply evolution equations for the macroscopic quantities.

Substituting these expansions into the lattice Boltzmann equation (14), we obtain

$$\left(\partial_{t_0} + \boldsymbol{\xi}_i \cdot \nabla\right) f_i^{(0)} = -\frac{1}{\tau} f_i^{(1)}, \tag{17a}$$

$$\partial_{t_1} f_i^{(0)} + \left(\partial_{t_0} + \boldsymbol{\xi}_i \cdot \nabla\right) f_i^{(1)} = -\frac{1}{\tau} f_i^{(2)}, \tag{17b}$$

at $O(1)$ and $O(\epsilon)$. The leading order continuity and momentum equations, (12a) and (12b) with $\nu = 0$, follow from taking the moments $\sum_{i=0}^{N}$ and $\sum_{i=0}^{N} \boldsymbol{\xi}_i$ of (17a), respectively,

$$\partial_{t_0}\rho + \nabla\cdot(\rho\mathbf{u}) = 0, \quad \partial_{t_0}(\rho\mathbf{u}) + \nabla\cdot\boldsymbol{\Pi}^{(0)} = 0. \tag{18}$$

The right hand sides vanish by virtue of the solvability conditions (16). Similarly, we obtain

$$\partial_{t_1}\rho = 0, \quad \partial_{t_1}(\rho\mathbf{u}) + \nabla\cdot\boldsymbol{\Pi}^{(1)} = 0, \tag{19}$$

at next order in ϵ, from moments of (17b) and the solvability conditions. Thus neglecting terms of $O(\epsilon^2)$, Eqs. (18) and (19) combine to give

$$\partial_t\rho + \nabla\cdot(\rho\mathbf{u}) = 0, \quad \partial_t(\rho\mathbf{u}) + \nabla\cdot\left(\boldsymbol{\Pi}^{(0)} + \epsilon\boldsymbol{\Pi}^{(1)}\right) = 0. \tag{20}$$

An equation for the first correction stress, $\boldsymbol{\Pi}^{(1)}$, follows from the second moment, $\sum_{i=0}^{N} \boldsymbol{\xi}_i\boldsymbol{\xi}_i$ of (17a),

$$\partial_{t_0}\boldsymbol{\Pi}^{(0)} + \nabla\cdot\left(\sum_{i=0}^{N}\boldsymbol{\xi}_i\boldsymbol{\xi}_i\boldsymbol{\xi}_i f_i^{(0)}\right) = -\frac{1}{\tau}\boldsymbol{\Pi}^{(1)}. \tag{21}$$

If we choose an equilibrium distribution $f_i^{(0)}$ with moments

$$\sum_{i=0}^{N} f_i^{(0)} = \rho, \quad \sum_{i=0}^{N}\boldsymbol{\xi}_i f_i^{(0)} = \rho\mathbf{u}, \quad \boldsymbol{\Pi}^{(0)} = \sum_{i=0}^{N}\boldsymbol{\xi}_i\boldsymbol{\xi}_i f_i^{(0)} = \theta\rho\mathsf{I} + \rho\mathbf{u}\mathbf{u}, \tag{22}$$

we recover the leading order ($\epsilon = 0$) continuity (12a) and momentum equations (12b) from (18). Comparing (22) with (12b), the equation of state is $p = \theta\rho$. Thus $\theta = c_s^2$ is the temperature in dimensionless variables in which Boltzmann's constant equals unity. The most common lattice Boltzmann equations make an isothermal (constant θ) approximation [17, 38, 64, 65, 72]. The isothermal approximation suffices to simulate weakly compressible fluids, since the associated error is $O(\mathrm{Ma}^2)$, like the compressibility error, and is manifested as an additional bulk viscosity [25].

An explicit formula for a distribution function with the correct moments is [17, 64]

$$f_i^{(0)} = \rho w_i\left(1 + \frac{\boldsymbol{\xi}_i\cdot\mathbf{u}}{\theta} + \frac{(\boldsymbol{\xi}_i\cdot\mathbf{u})^2}{2\theta^2} - \frac{\mathbf{u}^2}{2\theta}\right), \tag{23}$$

where the w_i are weights associated with the lattice speeds $\boldsymbol{\xi}_i$. The most common example is a two-dimensional nine-speed lattice with the temperature $\theta = 1/3$, and weights [17, 35, 36, 64]

$$w_i = \begin{cases} 4/9, & i = 0, \\ 1/9, & i = 1, 2, 3, 4, \\ 1/36, & i = 5, 6, 7, 8. \end{cases} \tag{24}$$

The velocity vectors, with magnitudes $|\boldsymbol{\xi}_i| = 1$ for $i = 1, 2, 3, 4$ and $|\boldsymbol{\xi}_i| = \sqrt{2}$ for $i = 5, 6, 7, 8$, form a square lattice, as illustrated in Fig. 1.

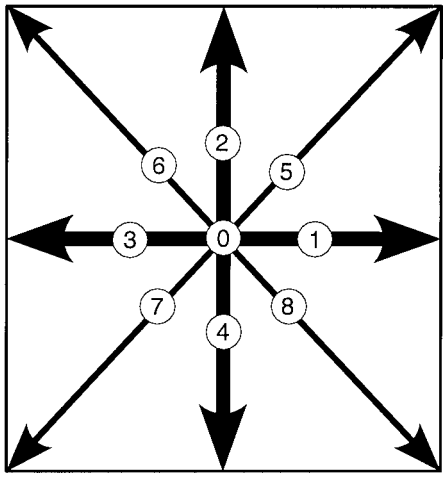

FIG. 1. The nine particle speeds used by the hydrodynamic lattice Boltzmann equation. Only the five speeds 0, 1, 2, 3, 4, shown with thick lines, are used for the magnetic field.

Since we can compute $\partial_{t_0}\mathbf{\Pi}^{(0)} = \partial_{t_0}(\theta\rho\mathsf{I} + \rho\mathbf{uu})$ from the known expressions (18) for $\partial_{t_0}\rho$ and $\partial_{t_0}(\rho\mathbf{u})$, (21) gives an explicit expression for $\mathbf{\Pi}^{(1)}$ in terms of ρ and $\mathbf{u}$ and their spatial derivatives. This is where the Chapman–Enskog expansion sidesteps the usual moment closure problem, since we can compute $\mathbf{\Pi}^{(0)}$ from the macroscopic variables ρ and $\mathbf{u}$ and their derivatives with respect to $\mathbf{x}$ and t. For the equilibrium distributions $f_i^{(0)}$ above, Eq. (21) simplifies to [24, 25, 38, 64]

$$\Pi^{(1)}_{\alpha\beta} = -\tau\theta\rho\,(\partial_\alpha u_\beta + \partial_\beta u_\alpha) + \tau\,\partial_{\beta\gamma}(\rho u_\alpha u_\beta u_\gamma), \tag{25}$$

which further simplifies to $\mathbf{\Pi}^{(1)} = -2\theta\tau\mathsf{S} + O(\mathrm{Ma}^3)$ in the low Mach number limit. Thus if we choose $\epsilon\tau = \nu/\theta$, the correct continuity and viscous Navier–Stokes momentum equations are recovered from the lattice scalar Boltzmann equation (14) in the limit of small mean free path ϵ. The $O(\rho u^3)$ term is an artifact of truncating the equilibrium distribution (23) at $O(u^2)$ [64] and may be removed by retaining more terms, at the expense of a larger lattice with 13 or 17 speeds rather than 9 [65, 72].

4. LORENTZ FORCE AND MAXWELL STRESSES

The inviscid ($\nu = 0$) momentum equation (11b) with a magnetic field may be rewritten in conservative form as [4, 48, 63]

$$\partial_t(\rho\mathbf{u}) + \nabla\cdot\left(p\mathsf{I} + \rho\mathbf{uu} + \frac{1}{2}B^2\mathsf{I} - \mathbf{BB}\right) = 0. \tag{26}$$

The Lorentz force $\mathbf{J}\times\mathbf{B}$ has been expressed as minus the divergence of the Maxwell stress tensor given by

$$M_{\alpha\beta} = \frac{1}{2}\delta_{\alpha\beta}|\mathbf{B}|^2 - B_\alpha B_\beta, \tag{27}$$

under the assumption that $\nabla\cdot\mathbf{B} = 0$. Thus the hydrodynamic lattice Boltzmann equation of the last section may be modified to include the Lorentz force by changing the second

moment, $\mathbf{\Pi}^{(0)} = \sum \boldsymbol{\xi}_i \boldsymbol{\xi}_i f_i^{(0)}$, of the equilibrium distribution function $f_i^{(0)}$ to be

$$\mathbf{\Pi}^{(0)} = \left(\theta\rho + \frac{1}{2}B^2\right)\mathsf{I} + \rho\mathbf{uu} - \mathbf{BB}, \tag{28}$$

while leaving the zeroth, $\rho = \sum f_i^{(0)}$, and first, $\rho\mathbf{u} = \sum \boldsymbol{\xi}_i f_i^{(0)}$, moments unchanged. An extra term with the required moments is

$$-w_i \frac{1}{2\theta^2}(\boldsymbol{\xi}_i\boldsymbol{\xi}_i - \theta\mathsf{I}) : (\mathsf{M} - \theta\mathsf{I}(\mathrm{Tr}\,\mathsf{M})), \tag{29}$$

based on expanding the equilibrium distribution in the orthogonal tensor Hermite polynomials $1, \boldsymbol{\xi}, \boldsymbol{\xi}\boldsymbol{\xi} - \theta\mathsf{I}, \ldots$ [24, 35, 36]. In two space dimensions, with $\mathbf{B} = (B_x, B_y, 0)$, a suitable equilibrium distribution is thus

$$f_i^{(0)} = w_i\rho\left(1 + \theta\boldsymbol{\xi}_i\cdot\mathbf{u} + \frac{1}{2\theta^2}(\boldsymbol{\xi}_i\cdot\mathbf{u})^2 - \frac{1}{2\theta}\mathbf{u}^2\right) + \frac{w_i}{2\theta^2}\left(\frac{1}{2}|\mathbf{B}|^2|\boldsymbol{\xi}_i|^2 - (\boldsymbol{\xi}_i\cdot\mathbf{B})^2\right), \tag{30}$$

although there are other equilibria with the same moments [23]. In two dimensions, the moments appearing in the Chapman–Enskog expansion apply only eight constraints, whereas the nine-speed lattice involves nine undetermined equlibrium distributions.

A body force $\mathbf{F}$, such as $\mathbf{F} = \mathbf{J}\times\mathbf{B}$ in (12b), gives rise to a spurious contribution $-\tau(\mathbf{Fu} + \mathbf{uF})$ to the viscous stress $\mathbf{\Pi}^{(1)}$ unless the second ($\boldsymbol{\xi}\boldsymbol{\xi}$) moment of the body force is treated correctly [24]. This is because the inviscid momentum equation is used to eliminate the time derivative of the leading order stress $\mathbf{\Pi}^{(0)}$ in favor of spatial derivatives, as outlined in the Appendix. In continuum kinetic theory these extra terms are canceled by terms coming from the second moment of the microscopic body force term $\rho^{-1}\mathbf{F}\cdot\nabla_{\boldsymbol{\xi}} f$ in the Boltzmann equation. If the body force $\mathbf{F}$ is known pointwise in terms of macroscopic variables, the spurious viscous stress may be eliminated by adding extra terms to the discrete body force [24]. However, the Lorentz force depends upon spatial *gradients* of the macroscopic variable $\mathbf{B}$. While it is possible to write the Lorentz force as the divergence of a stress, and so incorporate it into $f_i^{(0)}$, it is not possible to write the combination $\mathbf{Fu} + \mathbf{uF}$ as either a pointwise force or the divergence of a stress. Fortunately, in our scalings the spurious term is $O(\mathrm{Ma}^3/\mathrm{Re})$, so it is consistent to neglect it along with the usual $O(\rho u^3)$ term in (25) above. The scheme in this paper could be improved by including this extra stress, using the consistent approximation to the current $\mathbf{J} = \nabla\times\mathbf{B}$ at lattice points derived in (45a) and (45b). This may reduce the numerical magnitude of the errors at finite Mach number (see Section 9), although there would still be an $O(\mathrm{Ma}^3/\mathrm{Re})$ spurious viscous stress from $\nabla\cdot(\rho\mathbf{uuu})$, an $O(\mathrm{Ma}^3/\mathrm{Rm})$ error in the resistive term $\mathbf{\Lambda}^{(1)}$ due to $\partial_{t_0}\mathbf{\Lambda}^{(0)}$ (see the Appendix), and an $O(\mathrm{Ma}^2)$ compressibility error.

5. LATTICE KINETIC INDUCTION EQUATION

As explained in the Introduction, it is not possible to construct a kinetic formulation for the magnetic induction equation using a scalar distribution function in a way analogous to the use of the scalar Boltzmann–BGK equation to simulate the vector Navier–Stokes momentum equation. Instead, we introduce a vector-valued distribution function $\mathbf{g}_i(\mathbf{x}, t)$, as proposed by

Croisille *et al*. [21] and Bouchut [7] for continuous $\boldsymbol{\xi}$ and equate the macroscopic magnetic field vector $\mathbf{B}$ with the sum of the vector distribution function $\mathbf{g}_i$ over lattice vectors,

$$\mathbf{B} = \sum_{i=0}^{M} \mathbf{g}_i. \tag{31}$$

We propose that $\mathbf{g}_i(\mathbf{x}, t)$ should satisfy the vector Boltzmann–BGK equation

$$\partial_t \mathbf{g}_i + \Xi_i \cdot \nabla \mathbf{g}_i = -\frac{1}{\epsilon \tau_{\mathrm{m}}} \big(\mathbf{g}_i - \mathbf{g}_i^{(0)}\big), \tag{32}$$

for some vector-valued equilibrium distribution $\mathbf{g}_i^{(0)}$. We use an uppercase Ξ_i for the set of M lattice vectors in (32), with associated weights W_i and temperature Θ, to emphasise that the lattice used for (32) may differ from the lattice used for the hydrodynamic distribution functions f_i. However, the nodes of the two lattices should coincide so that we may transfer macroscopic quantities such as $\mathbf{u}$ and $\mathbf{B}$ between the two lattices without interpolation. We expect the equilibrium distribution $\mathbf{g}_i^{(0)}$ to depend upon $\mathbf{u}$, just as the hydrodynamic equilibrium distribution $f_i^{(0)}$ in (30) depends upon $\mathbf{B}$. The relaxation time τ_{m} in (32) may differ from the time τ in the hydrodynamic Boltzmann–BGK equation (14), so the electrical resistivity η may be adjusted independently of the fluid viscosity ν.

We included a small parameter ϵ in Eq. (32) to order the terms in a Chapman–Enskog expansion, which proceeds analogously to the expansion for the scalar lattice Boltzmann–BGK equation (14). We pose a multiple scale expansion of both $\mathbf{g}$ and t in powers of ϵ,

$$\mathbf{g} = \mathbf{g}^{(0)} + \epsilon \mathbf{g}^{(1)} + \epsilon^2 \mathbf{g}^{(2)} + \cdots, \quad \partial_t = \partial_{t_0} + \epsilon \partial_{t_1} + \cdots, \tag{33}$$

where again t_0 and t_1 are advective and diffusive timescales, respectively. We impose the single solvability condition

$$\sum_{i=0}^{M} \mathbf{g}_i^{(1)} = \sum_{i=0}^{M} \mathbf{g}_i^{(2)} = \cdots = 0. \tag{34}$$

In other words, the higher order terms do not contribute to the macroscopic magnetic field.

Substituting into the vector Boltzmann–BGK equation (32), we obtain

$$\big(\partial_{t_0} + \boldsymbol{\Xi}_i \cdot \nabla\big)\mathbf{g}_i^{(0)} = -\frac{1}{\tau_{\mathrm{m}}} \mathbf{g}_i^{(1)}, \tag{35a}$$

$$\partial_{t_1} \mathbf{g}_i^{(0)} + \big(\partial_{t_0} + \boldsymbol{\Xi}_i \cdot \nabla\big)\mathbf{g}_i^{(1)} = -\frac{1}{\tau_{\mathrm{m}}} \mathbf{g}_i^{(2)}, \tag{35b}$$

at $O(1)$ and $O(\epsilon)$. From $\sum_{i=0}^{M}$ of (35a) and (35b) we obtain an evolution equation for the macroscopic magnetic field $\mathbf{B}$ in the form

$$\partial_t B_\beta + \partial_\alpha \big(\boldsymbol{\Lambda}_{\alpha\beta}^{(0)} + \epsilon \boldsymbol{\Lambda}_{\alpha\beta}^{(1)}\big) = 0, \tag{36}$$

where the tensors $\boldsymbol{\Lambda}^{(0)}$, $\boldsymbol{\Lambda}^{(1)}, \ldots$, are defined by the first moments of $\mathbf{g}^{(0)}, \mathbf{g}^{(1)}, \ldots$,

$$\boldsymbol{\Lambda}_{\alpha\beta}^{(n)} = \sum_{i=0}^{M} \Xi_{i\alpha} g_{i\beta}^{(n)}, \quad \text{for } n = 0, 1, \ldots. \tag{37}$$

The detailed derivation follows the derivation of the momentum equation (20) above. From $\sum_{i=0}^{M} \Xi_{i\alpha}$ of (35a) we obtain an equation analogous to (21) for the first correction $\mathbf{\Lambda}^{(1)}$,

$$\partial_{t_0} \Lambda^{(0)}_{\alpha\beta} + \partial_\gamma \left(\sum_{i=0}^{M} \Xi_{i\gamma} \Xi_{i\alpha} g^{(0)}_{i\beta} \right) = -\frac{1}{\tau_\mathrm{m}} \Lambda^{(1)}_{\alpha\beta}. \tag{38}$$

Equation (36) with $\epsilon = 0$ will coincide with the ideal MHD induction equation (11b) if we choose an equilibrium distribution $g^{(0)}_{i\beta}$ with the moments

$$\sum_{i=0}^{M} g_{i\beta} = B_\beta, \tag{39}$$

$$\Lambda^{(0)}_{\alpha\beta} = \sum_{i=0}^{M} \Xi_{i\alpha} g^{(0)}_{i\beta} = u_\alpha B_\beta - B_\alpha u_\beta. \tag{40}$$

The simplest choice is

$$g^{(0)}_{i\beta} = W_i [B_\beta + \Theta^{-1} \Xi_{i\alpha} (u_\alpha B_\beta - B_\alpha u_\beta)], \tag{41}$$

where the Ξ_i and W_i are the vectors and weights of a symmetric lattice satisfying

$$\sum_{i=0}^{M} W_i = 1, \quad \sum_{i=0}^{M} W_i \Xi_{i\alpha} \Xi_{i\beta} = \Theta \delta_{\alpha\beta}. \tag{42}$$

The symmetry of the lattice ensures that the first and third moments vanish automatically, $\sum_i W_i \Xi_{i\alpha} = 0$ and $\sum_i W_i \Xi_{i\alpha} \Xi_{i\beta} \Xi_{i\gamma} = 0$. For the equilibrium distribution (41) we find

$$\sum_{i=0}^{M} \Xi_{i\gamma} \Xi_{i\alpha} g^{(0)}_{i\beta} = \Theta \delta_{\gamma\alpha} B_\beta, \tag{43}$$

so Eq. (38) implies that

$$\Lambda^{(1)}_{\alpha\beta} = -\Theta \tau_\mathrm{m} \partial_\alpha B_\beta + O(\mathrm{Ma}^3), \tag{44}$$

where the $O(\mathrm{Ma}^3)$ term is due to $\partial_{t_0} \mathbf{\Lambda}^{(0)}$ (see the Appendix). Thus the macroscopic equation (36) is the required resistive magnetic induction equation (11b), with an error of $O(\mathrm{Ma}^3/\mathrm{Rm})$, provided we choose $\epsilon \tau_m = \eta/\Theta$. We note that $\mathbf{\Lambda}^{(1)}$ is not antisymmetric because $\partial_\alpha B_\beta \neq \partial_\beta B_\alpha$ in general. However, the missing term vanishes when we compute $\partial_\alpha \Lambda^{(1)}_{\alpha\beta}$, since $\partial_\alpha \partial_\beta B_\alpha = \partial_\beta \nabla \cdot \mathbf{B} = 0$. Thus this system simulates the induction equation in the form appearing in (12c), rather than the original explicitly antisymmetric form in (11b) (see Section 6). Equation (44) provides consistent approximations to $\nabla \cdot \mathbf{B}$ and $\mathbf{J} = \nabla \times \mathbf{B}$,

$$\mathrm{Tr} \mathbf{\Lambda} = \Lambda_{\alpha\alpha} = -\Theta \tau_\mathrm{m} \nabla \cdot \mathbf{B} + O\left(\tau_\mathrm{m}^2\right), \tag{45a}$$

$$\epsilon_{\alpha\beta\gamma} \left(\Lambda_{\alpha\beta} - \Lambda^{(0)}_{\alpha\beta} \right) = -\Theta \tau_\mathrm{m} (\nabla \times \mathbf{B})_\gamma + O\left(\tau_\mathrm{m}^2\right) + O(\mathrm{Ma}^3). \tag{45b}$$

The $O(\mathrm{Ma}^3)$ term vanishes from $\mathrm{Tr} \mathbf{\Lambda}$ since it simplifies to $\partial_{t_0} \mathrm{Tr} \mathbf{\Lambda}^{(0)}$, and $\mathrm{Tr} \mathbf{\Lambda}^{(0)} = 0$.

As the fourth-order lattice tensor $\sum W_i \, \Xi_i \, \Xi_i \, \Xi_i \, \Xi_i$ is not required in deriving the induction equation, we may use a lattice with less symmetry than the nine-speed lattice needed for an isotropic viscous momentum equation. In two dimensions we used a five-point lattice with weights

$$W_0 = \frac{1}{3}, \quad W_i = \frac{1}{6}, \quad \text{for } i = 1, 2, 3, 4, \tag{46}$$

for which $\Theta = 1/3$, the same as θ for the nine-point lattice (24) used in the two-dimensional momentum equation. These speeds are illustrated in Fig. 1, where only the thick lines are used for the magnetic field. This permits a substantial saving in storage, partly compensating for the need to associated a vector-valued distribution function with each lattice speed.

We also tried an alternative four-point lattice omitting the zero speed,

$$W_i = \frac{1}{4}, \quad \text{for } i = 1, 2, 3, 4. \tag{47}$$

This lattice satisfies (42) with $\Theta = \frac{1}{2}$. For given flow parameters and grid resolution, simulations with this lattice proved notably less stable than with the five-point lattice. For example, the doubly periodic coalescence simulation with $\eta = \nu = 0.004$ was unstable on a 256×256 grid when using only four lattice speeds but was stable with five speeds. This is as expected by analogy with lattice Boltzmann hydrodynamics, where including "rest particles" with zero speed substantially improves the stability of simulations at larger Reynolds numbers for a given spatial resolution [14]. There may be further scope for optimizing the lattice weights W_i (and also Θ) beyond the two choices in (46) and (47).

As noted above, the equilibrium distribution (41) in fact leads to a perturbation electric field tensor $\mathbf{\Lambda}^{(1)}$ that is not antisymmetric. Thus we approximate the continuum induction equation as it appears in (12c), rather than the explicitly antisymmetric form (11b). From the divergence of (12c) we find that $\nabla \cdot \mathbf{B}$ satisfies the diffusion equation

$$\partial_t (\nabla \cdot \mathbf{B}) = \eta \nabla^2 (\nabla \cdot \mathbf{B}), \tag{48}$$

instead of $\partial_t \nabla \cdot \mathbf{B} = 0$. This difference is probably only beneficial since at worst we might expect $\nabla \cdot \mathbf{B}$ to be generated with alternating sign at small scales [71], which will quickly cancel out through diffusion, and $\mathbf{\Lambda}^{(0)} + \mathbf{\Lambda}^{(1)}$ in fact coincides with the tensor proposed in [43] for writing the induction equation in divergence form.

In any case, it is not possible to modify the equilibrium distribution in our formulation to make $\mathbf{\Lambda}^{(1)}$ antisymmetric. A natural idea is to try to modify $g_i^{(0)}$ so that (43) becomes

$$\sum_{i=0}^{M} \Xi_{i\gamma} \, \Xi_{i\alpha} \, g_{i\beta}^{(0)} = \Theta (\delta_{\gamma\alpha} B_\beta - \delta_{\gamma\beta} B_\alpha), \tag{49}$$

which is antisymmetric under the interchange of α and β. However, the right hand side is not symmetric under the interchange of α and γ, whereas the left hand side must have this symmetry by construction. The expression on the left hand side cannot be both symmetric under ($\alpha \leftrightarrow \gamma$) and antisymmetric under ($\alpha \leftrightarrow \beta$) without vanishing completely.

6. MAINTAINING $\nabla \cdot \mathbf{B} = 0$

As explained in the introduction, the structure of the magnetic induction equation implies that $\partial_t \nabla \cdot \mathbf{B} = 0$. Since $\nabla \cdot \mathbf{B} = 0$ in the initial conditions, $\nabla \cdot \mathbf{B}$ should remain zero subsequently. From the traces of (40) and (38) we find that $\mathrm{Tr}\boldsymbol{\Lambda}^{(0)} = 0$ and $\mathrm{Tr}\boldsymbol{\Lambda}^{(1)} = -\Theta\tau_\mathrm{m}\nabla \cdot \mathbf{B}$. The $O(\mathrm{Ma}^3)$ term in (44) vanishes exactly upon taking the trace, since it is the time derivative of the traceless tensor $\boldsymbol{\Lambda}^{(0)}$. Thus the divergence-free condition $\nabla \cdot \mathbf{B} = 0$ is equivalent to $\mathrm{Tr}\boldsymbol{\Lambda} = 0$ to the first two orders in the Chapman–Enskog expansion. Since we are ignoring Burnett-like effects at higher order beyond the viscous Navier–Stokes equations [11, 12, 32], it is consistent to approximate the constraint $\nabla \cdot \mathbf{B} = 0$ using the constraint $\mathrm{Tr}\boldsymbol{\Lambda} = 0$.

In numerical experiments $\mathrm{Tr}\boldsymbol{\Lambda} = 0$ was maintained to machine round-off error, typically $|\mathrm{Tr}\boldsymbol{\Lambda}| < 10^{-16}$, using 64-bit (17 digit) IEEE floating point arithmetic. We also constructed spectrally accurate approximations to $\nabla \times \mathbf{B}$ and $\nabla \cdot \mathbf{B}$ from $\mathbf{B}$ evaluated at lattice points. The spectral approximation to $\nabla \cdot \mathbf{B}$ differed from zero by an amount proportional to the square of the lattice spacing, because $\mathrm{Tr}\boldsymbol{\Lambda} = 0$ is a consistent, and thus only second-order accurate, approximation to $\nabla \cdot \mathbf{B} = 0$. However, we still found $\nabla \cdot \mathbf{B} \ll |\nabla \times \mathbf{B}|$ even in regions of high current concetration, as shown in Table III below.

Some explanation for why $\mathrm{Tr}\boldsymbol{\Lambda} = 0$ is maintained to machine round-off error, rather than merely to spatial truncation error, may be gained by examining higher order terms in the Chapman–Enskog expansion. From the trace of (35b) we obtain

$$\mathrm{Tr}\,\boldsymbol{\Lambda}^{(2)} = 2\Theta\tau_\mathrm{m}^2\partial_{t_0}\nabla \cdot \mathbf{B} = 0, \tag{50}$$

since $\partial_{t_0}\nabla \cdot \mathbf{B} = \nabla\nabla\colon(\mathbf{Bu} - \mathbf{uB}) = 0$. Thus $\mathrm{Tr}\boldsymbol{\Lambda} = -\tau_\mathrm{m}\Theta\nabla \cdot \mathbf{B} + O(\tau_\mathrm{m}^3)$, rather than $+ O(\tau_\mathrm{m}^2)$ as originally expected. Carrying the expansion leading to equations (35a) and (35b) to one higher order,

$$\partial_{t_2}\mathbf{g}_i^{(0)} + \partial_{t_1}\mathbf{g}_i^{(1)} + \left(\partial_{t_0} + \Xi_i \cdot \nabla\right)\mathbf{g}_i^{(2)} = -\frac{1}{\boldsymbol{\tau}_\mathrm{m}}\mathbf{g}_i^{(3)}, \tag{51}$$

we also obtain

$$\begin{aligned}\mathrm{Tr}\boldsymbol{\Lambda}^{(3)} &= 2\tau_\mathrm{m}^2\Theta\partial_{t_1}\nabla \cdot \mathbf{B} - \tau_\mathrm{m}^3\partial_\alpha\partial_\beta\partial_\gamma\sum_{i=0}^{M} W_i\,\Xi_{i\alpha}\,\Xi_{i\beta}\,\Xi_{i\gamma}\,\Xi_{i\mu}B_\mu \\ &= 2\tau_\mathrm{m}^3\Theta^2\nabla^2\nabla \cdot \mathbf{B} - \Theta\tau_\mathrm{m}^3\left(\frac{\partial^3 B_x}{\partial x^3} + \frac{\partial^3 B_y}{\partial y^3}\right),\end{aligned} \tag{52}$$

for the five-speed lattice in (46). We have also used $\partial_{t_1}(\nabla \cdot \mathbf{B}) = \Theta\tau_\mathrm{m}\nabla^2\nabla \cdot \mathbf{B}$ from (48). The lack of isotropy of the fourth lattice tensor appearing in (52) is evident from the form of the second term, which is why this lattice is not suitable for lattice Boltzmann hydrodynamics with an isotropic viscous stress. However, $\mathrm{Tr}\boldsymbol{\Lambda}^{(3)}$ comprises derivatives of $\nabla \cdot \mathbf{B}$, which should be small, multiplied by the third power of the small parameter τ, the mean free path, so it is reasonable to expect that it would be lost in the numerical rounding error, as found experimentally.

Powell [63; see also 48] proposed including source terms proportional to $\nabla \cdot \mathbf{B}$ in the induction, momentum, and energy equations. These terms are supposed to reduce the undesirable influence of spurious magnetic monopoles on the rest of the solution by allowing

them to advect away from any regions where they might be formed. In particular, Powell proposed the induction equation

$$\partial_t \mathbf{B} + \nabla \cdot (\mathbf{uB} - \mathbf{Bu}) = -\mathbf{u}\nabla \cdot \mathbf{B}, \tag{53}$$

in the ideal case ($\eta = 0$), which implies a passive advection equation for $\nabla \cdot \mathbf{B}$. Janhunen [42] recently suggested that only the induction equation should be modified, which preserves energy and momentum conservation (see [26] for further justification). Either scheme could be readily incorporated via source terms in the induction, and possibly momentum, equations since we have a consistent approximation to $\nabla \cdot \mathbf{B}$ available at lattice points from $\mathrm{Tr}\mathbf{\Lambda}$. However, such a modification does not seem to be necessary based on the two-dimensional simulations presented below.

7. REDUCTION TO FULLY DISCRETE FORM

To achieve a fully discrete system suitable for computations we must approximate (14) and (32) in $\mathbf{x}$ and t, as well as in $\boldsymbol{\xi}$. Integrating (14) along a characteristics for a time interval Δt, we obtain

$$f_i(\mathbf{x}+\boldsymbol{\xi}_i\Delta t, t+\Delta t) - f_i(\mathbf{x}, t) = \int_0^{\Delta t} -\frac{1}{\tau}\big(f_i(\mathbf{x}+\boldsymbol{\xi}_i s, t+s) - f_i^{(0)}(\mathbf{x}+\boldsymbol{\xi}_i s, t+s)\big), \tag{54}$$

and a similar equation for each vector component of (32). The integral on the right hand side of (54) may be approximated with second-order accuracy using the trapezium rule,

$$\begin{aligned} -\frac{1}{\tau}\int_0^{\Delta t} f_i(\mathbf{x}+\boldsymbol{\xi}_i s, t+s)\, ds = -\frac{1}{\tau}\frac{\Delta t}{2}\big(&f_i(\mathbf{x}+\boldsymbol{\xi}_i\Delta t, t+\Delta t) - f_i^{(0)}(\mathbf{x}+\boldsymbol{\xi}_i\Delta t, t+\Delta t) \\ &+ f_i(\mathbf{x}, t) - f_i^{(0)}(\mathbf{x}, t)\big) + O(\Delta t^3). \end{aligned} \tag{55}$$

Unfortunately, the $f_i^{(0)}(\mathbf{x}+\boldsymbol{\xi}_i\Delta t, t+\Delta t)$ terms are not known in advance, since they depend on $f_i(\mathbf{x}+\boldsymbol{\xi}_i\Delta t, t+\Delta t)$ and $\mathbf{g}_i(\mathbf{x}+\boldsymbol{\xi}_i\Delta t, t+\Delta t)$ via ρ, $\mathbf{u}$, and $\mathbf{B}$ evaluated at $t+\Delta t$. Thus a straightforward combination of (55) and (54) yields a set of coupled nonlinear algebraic equations which must be solved to find the f_i and $\mathbf{g}_i$ at time $t+\Delta t$. However, this system of equations may be rendered fully explicit by a change of variables [34, 37]. We introduce a new set of distribution functions $\bar{f}_i$ and $\bar{\mathbf{g}}_i$ defined by

$$\bar{f}_i(\mathbf{x}, t) = f_i(\mathbf{x}, t) + \frac{\Delta t}{2\tau}\big(f_i(\mathbf{x}, t) - f_i^{(0)}(\mathbf{x}, t)\big), \tag{56a}$$

$$\bar{\mathbf{g}}_i(\mathbf{x}, t) = \mathbf{g}_i(\mathbf{x}, t) + \frac{\Delta t}{2\tau_{\mathrm{m}}}\big(\mathbf{g}_i(\mathbf{x}, t) - \mathbf{g}_i^{(0)}(\mathbf{x}, t)\big). \tag{56b}$$

In these new variables the scheme defined by Eqs. (14), (32), and (55) is algebraically equivalent to the fully explicit scheme

$$\bar{f}_i(\mathbf{x}+\boldsymbol{\xi}_i\Delta t, t+\Delta t) = \bar{f}_i(\mathbf{x}, t) - \frac{\Delta t}{\tau + \Delta t/2}\big(\bar{f}_i(\mathbf{x}, t) - f^{(0)}(\mathbf{x}, t)\big), \tag{57a}$$

$$\bar{\mathbf{g}}_i(\mathbf{x}+\boldsymbol{\xi}_i\Delta t, t+\Delta t) = \bar{\mathbf{g}}_i(\mathbf{x}, t) - \frac{\Delta t}{\tau_{\mathrm{m}} + \Delta t/2}\big(\bar{\mathbf{g}}_i(\mathbf{x}, t) - \mathbf{g}^{(0)}(\mathbf{x}, t)\big), \tag{57b}$$

which is the one we used computationally. The macroscopic variables appearing in the equilibria $f_i^{(0)}$ and $\mathbf{g}_i^{(0)}$ defined by (30) and (41) are readily reconstructed from moments of the new distribution functions,

$$\rho = \sum_{i=0}^{8} \bar{f}_i, \quad \rho \mathbf{u} = \sum_{i=0}^{8} \boldsymbol{\xi}_i \bar{f}_i, \quad \left(1 + \frac{\Delta t}{2\tau}\right) \boldsymbol{\Pi} = \sum_{i=0}^{8} \boldsymbol{\xi}_i \boldsymbol{\xi}_i \bar{f}_i + \frac{\Delta t}{2\tau} \boldsymbol{\Pi}^{(0)}, \tag{58a}$$

$$\mathbf{B} = \sum_{i=0}^{4} \bar{\mathbf{g}}_i, \quad \left(1 + \frac{\Delta t}{2\tau_\mathrm{m}}\right) \boldsymbol{\Lambda}_{\alpha\beta} = \sum_{i=0}^{4} \Xi_{i\alpha} \bar{g}_{i\beta} + \frac{\Delta t}{2\tau_\mathrm{m}} \boldsymbol{\Lambda}^{(0)}_{\alpha\beta}. \tag{58b}$$

We describe numerical experiments using this scheme in the next two sections.

8. HARTMANN FLOW

Hartmann flow comprises a steady unidirectional flow of viscous, electrically conducting fluid through a channel containing a transverse magnetic field. It is the MHD analogue of plane Poiseuille flow in ordinary hydrodynamics, and like Poiseuille flow the nonlinear terms vanish for this flow geometry. It is thus one of the few analytically tractable MHD flows, with steady solutions of the form $\mathbf{u} = (0, u(x), 0)$, $\mathbf{B} = (B_0, b(x), 0)$, and $\rho = \rho(x)$. In the incompressible limit, the MHD equations for Hartmann flow simplify to two linear equations [54, 67],

$$0 = F + \rho_0 \nu \frac{d^2 u}{dx^2} + B_0 \frac{db}{dx}, \quad 0 = B_0 \frac{du}{dx} + \eta \frac{d^2 b}{dx^2}, \tag{59}$$

where F denotes a spatially uniform forcing in the along-channel direction, such as a pressure gradient. Assuming rigid and imperfectly conducting boundary conditions, so that u and b both vanish on $x = \pm L$, the system (59) has the exact solution

$$b(x) = \frac{FL}{B_0} \left(\frac{\sinh(Hx/L)}{\sinh(H)} - \frac{x}{L} \right), \quad u(x) = \frac{FL}{\sqrt{\rho_0} B_0} \sqrt{\frac{\eta}{\nu}} \coth(H) \left(1 - \frac{\cosh(Hx/L)}{\cosh(H)} \right). \tag{60}$$

The dimensionless parameter $H = B_0 L / \sqrt{\rho_0 \eta \nu}$ is the Hartmann number, which measures the ratio of Lorentz to viscous forces. When the Hartmann number is large, as is typical in liquid metal MHD applications, the magnetic field maintains a nearly uniform velocity u over the bulk of the channel [67]. The flow adjusts to the no-slip boundary conditions via thin Hartmann boundary layers of width $O(1/H)$ located at the two walls $x = \pm L$. Conversely, the flow approaches the parabolic Poiseuille profile $u(x) = (L^2 - x^2) F / (2\nu\rho_0)$ for small Hartmann numbers and weak magnetic fields.

The flow along the channel was driven by an imposed additional stress $xF(\hat{\mathbf{x}}\hat{\mathbf{y}} + \hat{\mathbf{y}}\hat{\mathbf{x}})$, whose divergence gives the required body force $F\hat{\mathbf{y}}$. The corresponding equilibrium distribution,

$$f_i^{(0)} = w_i \rho \left(1 + \theta \boldsymbol{\xi}_i \cdot \mathbf{u} + \frac{1}{2\theta^2} (\boldsymbol{\xi}_i \cdot \mathbf{u})^2 - \frac{1}{2\theta} \mathbf{u}^2 \right) + \frac{w_i}{2\theta^2} \left(\frac{1}{2} |\mathbf{B}|^2 |\boldsymbol{\xi}_i|^2 - (\boldsymbol{\xi}_i \cdot \mathbf{B})^2 \right) - \frac{w_i}{\theta^2} F x \boldsymbol{\xi}_{ix} \boldsymbol{\xi}_{iy}, \tag{61}$$

contains an extra term for a driving stress, as well as the Maxwell stress term in (30).

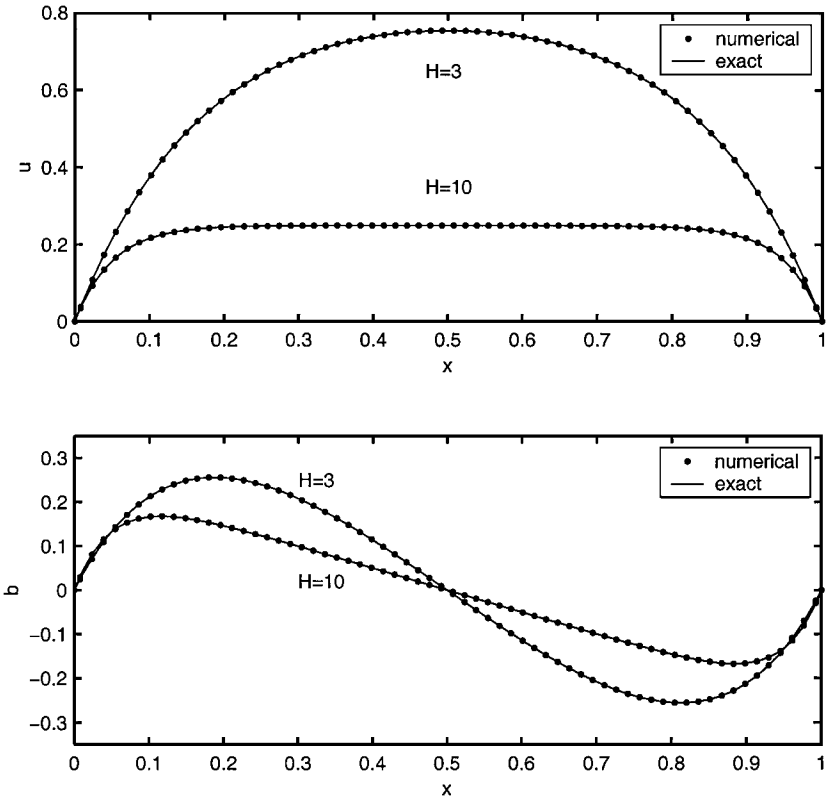

FIG. 2. Streamwise velocity and magnetic field in Hartmann flow. The dots (●) are from numerical simulations with 64 points, and the solid lines are exact incompressible solutions. When the Hartmann number $H = B_0 L/\sqrt{\rho_0 \eta \nu}$ is large, the flow is uniform outside Hartmann layers of thickness $H^{-1/2}$ at the walls.

Velocity boundary conditions were imposed using the bounce-back method [17, 38], placing the effective boundary half a lattice spacing outside the lattice point at which it is applied. The magnetic boundary conditions also used the bounce-back method, but with the sign reversed to enforce $b(x) = 0$ at $x = \pm L$. Some results are shown in Fig. 2. We had to take the Mach number $\mathrm{Ma} \propto \Delta x$ to establish second-order convergence to the incompressible solution (60), since the compressibility error is $O(\mathrm{Ma}^2)$ and the spatial truncation error is $O(\Delta x^2)$. There is also an $O(\mathrm{Ma}^2/\mathrm{Re})$ error in the viscous stress due to the uniform driving force (see Section 4 and [24]).

9. REDUCED MAGNETOHYDRODYNAMICS

Many important physical processes may be modeled by the two-dimensional incompressible "reduced" magnetohydrodynamic equations [4, 27, 50, 51]. These equations may be reformulated as two scalar equations by writing $\mathbf{u} = \hat{\mathbf{z}} \times \nabla\varphi = (-\partial_y\varphi, \partial_x\varphi, 0)$, and $\mathbf{B} = \hat{\mathbf{z}} \times \nabla\psi = (-\partial_y\psi, \partial_x\psi, 0)$, where φ and ψ are the streamfunction and magnetic flux function, respectively [4, 20, 58]. These representations automatically satisfy $\nabla \cdot \mathbf{u} = 0$ and $\nabla \cdot \mathbf{B} = 0$. The vorticity and electric current lie purely in the z direction, so we have $\nabla \times \mathbf{u} = \omega\hat{\mathbf{z}}$ and $\nabla \times \mathbf{B} = j\hat{\mathbf{z}}$, with $\omega = \nabla^2\varphi$ and $j = \nabla^2\psi$. The conventions which use ψ for the magnetic flux function, and the plus sign in $\omega = +\nabla^2\varphi$, are standard in reduced MHD, despite the unfortunate conflict with common, purely hydrodynamic usage.

With these definitions, the incompressible MHD equations (11a) and (11b) become

$$\partial_t \omega + [\varphi, \omega] = [\psi, j] + \nu \nabla^2 \omega, \tag{62a}$$

$$\partial_t \psi + [\varphi, \psi] = \eta \nabla^2 \psi, \tag{62b}$$

where the Jacobian or Poisson bracket is $[\varphi, \omega] = (\partial_x \varphi)(\partial_y \omega) - (\partial_y \varphi)(\partial_x \omega)$. The vorticity equation (62a) differs from the two-dimensional Navier–Stokes equations through the appearance of a source term $[\psi, j]$ due to the Lorentz force. This term loosely resembles the vortex-stretching term present in the three-dimensional Navier–Stokes vorticity equation, so in some ways the qualitative behavior of the 2D MHD equations more closely resembles that of the 3D Navier–Stokes equations than the 2D Navier–Stokes equations [4, 6, 33, 62]. For instance, the peak vorticity may grow exponentially in the 2D ideal MHD equations [33], whereas it is bounded by the initial peak vorticity in the 2D Euler and Navier–Stokes equations. Thus in 2D MHD turbulence the energy dissipation rate may attain a nonzero limit at high Reynolds numbers [4, 6], whereas in 2D hydrodynamic turbulence the energy dissipation rate is known to be $O(\mathrm{Re}^{-1})$.

9.1. Orszag–Tang Vortex

The Orszag–Tang vortex [58] is a two-dimensional flow evolving from simple deterministic initial conditions, namely

$$\varphi = 2(\cos(x) - \sin(y)), \quad \psi = 2\cos(x) - \cos(2y), \tag{63}$$

in the periodic domain $0 \leq x, y \leq 2\pi$. This flow nevertheless contains most of the features of MHD turbulence, notably selective decay, magnetic reconnection, formation of jets, and dynamic alignment. The deterministic initial conditions allow a direct comparison with previously published computations [20, 22, 58, 60–62, 71]. Moreover, the compressible analogue of the Orszag–Tang vortex has already been studied in the subsonic [22] and supersonic [60] regimes, so we may identify finite-compressibility features in the lattice kinetic simulations.

We performed simulations of the compressible isothermal Orszag–Tang vortex with $\nu = \eta = 0.02$ on 128^2, 256^2, and 512^2 grids at various Mach numbers. The nominal Reynolds numbers based on the initial velocity were $\mathrm{Re} = \mathrm{Rm} \approx 628$. We also computed solutions of the incompressible Orszag–Tang vortex using a conventional Fourier spectral collocation method with no dealiasing [8, 10, 22, 61, 62]. The nonlinear terms in the spectral method were integrated in time using fourth-order Runge–Kutta, while the linear diffusive terms were treated exactly using integrating factors, as with the linear propagator method used in [39]. This is only possible because Fourier modes are eigenfunctions of the diffusion operators, so the $\exp(-\eta|\mathrm{k}|^2 t)$ decay of each Fourier mode may be treated analytically by a change of variables.

The lower portions of Tables I and II show the expected exponential spatial convergence of a well-resolved spectral solution. Comparisons between different grids were performed on the coarse grid by pointwise coarsening of the fine-grid solution. The timestep was made sufficiently short that the temporal integration error in the 512^2 run was less than the difference between the 256^2 and 512^2 runs. Thus even the 128^2 the spectral solutions are effectively "exact" solutions, for the purpose of comparison with results computed using the lattice kinetic scheme.

TABLE I
Spatial Convergence: l_2 Errors at $t = 0.5$ between Kinetic and Spectral Solutions

Grid	Vorticity ω	Current j	Current from $\mathbf{\Lambda}^{(1)}$
128^2 kinetic–128^2 spectral	0.2486	0.3770	0.1788
256^2 kinetic–256^2 spectral	0.0550	0.0931	0.0400
512^2 kinetic–512^2 spectral	0.0132	0.0220	0.0088
128^2 spectral–256^2 spectral	1.7×10^{-6}	2.2×10^{-6}	
256^2 spectral–512^2 spectral	3.1×10^{-11}	3.2×10^{-11}	

Note. Discrete l_2 norm of the differences between vorticities and currents computed by the kinetic and spectral methods at $t = 0.5$. The last two rows show that even the 128^2 spectral solution is effectively exact compared with the spatial truncation error in the lattice kinetic scheme. The last two differences, between two different resolutions, were computed by projecting onto the coarser grid. The top three rows confirm the expected second-order spatial accuracy of the lattice kinetic scheme.

Tables I and II show that the spatial convergence of the lattice kinetic scheme is second order, as expected. These simulations were all performed with $\mathrm{Ma} = \sqrt{3}/50$, for which the error due to finite compressibility is much smaller than the spatial truncation error, as shown in Tables IV–VI below. The columns labeled "Vorticity ω" and "Current j" denote quantities constructed from the primitive variables $\mathbf{u}$ and $\mathbf{B}$ at lattice points by spectrally accurate differentiation. These are the quantities plotted in Fig. 3. The right hand columns labeled "Current from $\mathbf{\Lambda}^{(1)}$" refer to a current computed locally at lattice points from the nonequilibrium part of the electric field tensor $\mathbf{\Lambda}$ using (45b). The error in the current obtained from $\mathbf{\Lambda}^{(1)}$ appears to be consistently about half that of the error in the current obtained by differentiating $\mathbf{B}$, although the order of convergence is the same. The errors at $t = 1.0$ are systematically larger than those at $t = 0.5$ due to the formation of thin layers with large currents and vorticities (see Fig. 3). Table III shows that the approximation to $\nabla \cdot \mathbf{B}$ computed by spectrally differentiating $\mathbf{B}$ is proportional to Δx^2. This is as expected since the scheme is second-order accurate and conserved the consistent approximation $\mathrm{Tr}\mathbf{\Lambda} = 0$ to numerical round-off error.

We also investigated the errors due to finite Mach number, or finite compressibility. Tables IV–VI show the discrete l_2 differences in vorticity and current between simulations

TABLE II
Spatial Convergence: l_2 Errors at $t = 1.0$ between Kinetic and Spectral Solutions

Grid	Vorticity ω	Current j	Current from $\mathbf{\Lambda}^{(1)}$
128^2 kinetic–128^2 spectral	1.9302	2.1296	1.0295
256^2 kinetic–256^2 spectral	0.5985	0.5483	0.2254
512^2 kinetic–512^2 spectral	0.1531	0.1364	0.0544
128^2 spectral–256^2 spectral	0.0191	0.0149	
256^2 spectral–512^2 spectral	2.4×10^{-7}	8.2×10^{-8}	

Note. Discrete l_2 norm of the differences between vorticities and currents computed by the kinetic and spectral methods at $t = 1.0$. The last two rows show that even the 128^2 spectral solution is effectively exact compared with the spatial truncation error in the lattice kinetic scheme. The last two differences, between two different resolutions, were computed by projecting onto the coarser grid. The top three rows confirm the expected second-order spatial accuracy of the lattice kinetic scheme.

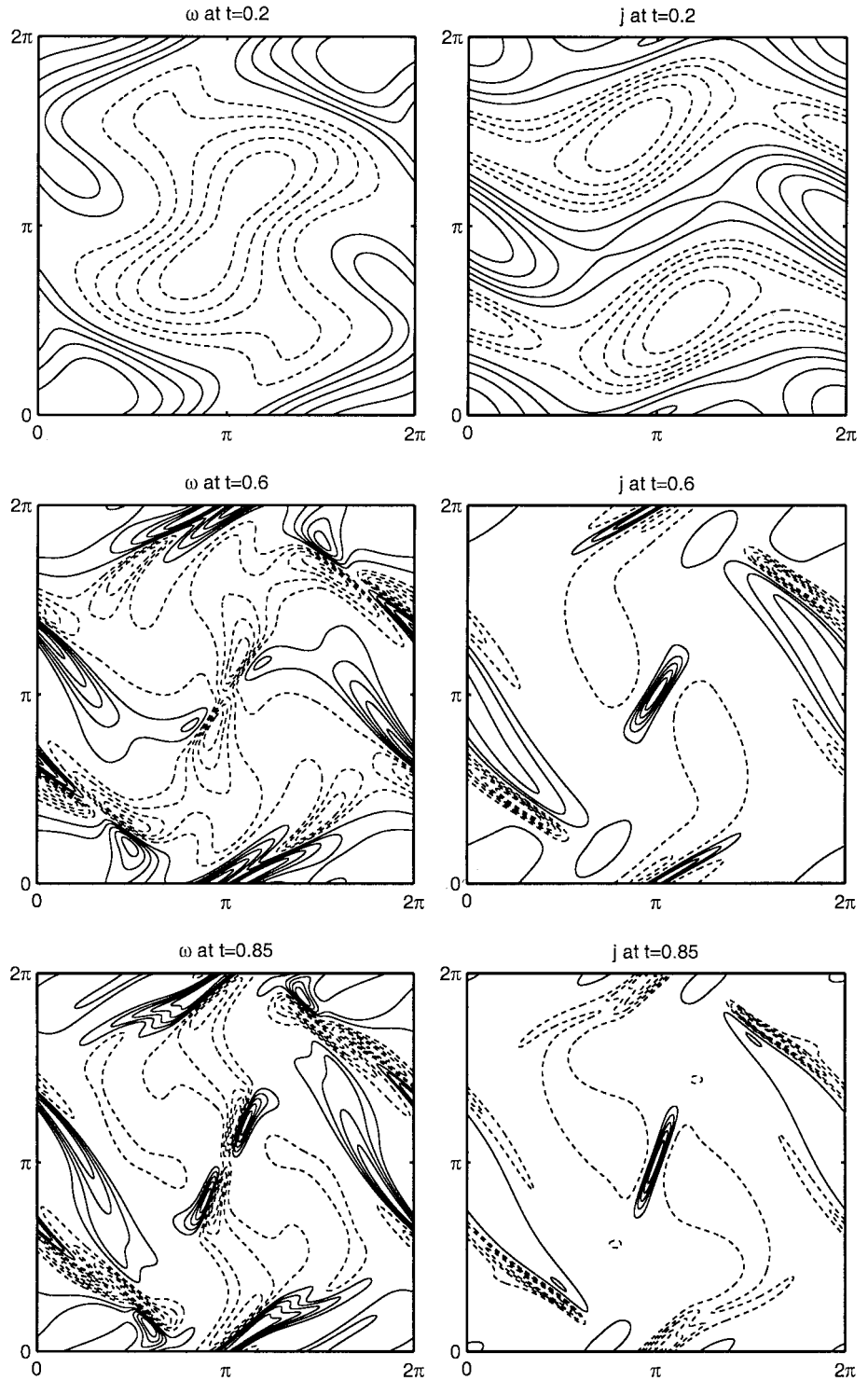

FIG. 3. Vorticity and current for the Orszag–Tang vortex. Positive contours are solid lines; negative contours are dotted lines. This figure should be compared with the inviscid, perfectly conducting computations in Fig. 1 of [33]. The flow at $t = 0.85$ is visibly affected by our finite resistivity and viscosity, whereas the computations in [33] were inviscid and perfectly conducting ($\eta = \nu = 0$).

TABLE III
Spatial Convergence: Maxima of $|\nabla \times \mathbf{u}|$, $|\nabla \times \mathbf{B}|$, and $|\nabla \cdot \mathbf{B}|$ Computed Spectrally

t	Grid	Vorticity ω	Current j	Spectral $\nabla \cdot \mathbf{B}$
0.5	128^2	6.744	17.96	0.0939
	256^2	6.754	18.20	0.0246
	512^2	6.758	18.24	0.0062
1.0	128^2	14.07	45.13	0.5642
	256^2	14.16	46.30	0.1611
	512^2	14.20	46.59	0.0415

at various Mach numbers on a fixed grid. These Mach numbers were chosen to be $\sqrt{3}/n$, based on the initial maximum velocity $|\mathbf{u}|_{\max} = 2$, which ensures that $t = 0.05$ precisely after an integer number of steps of length Δt. The differences shown are the discrete l_2 differences between simulations at Ma and Ma/2. The convergence rates were computed from successive pairs of differences, symbolically from the ratio $(\mathrm{Ma} - \mathrm{Ma}/2)/(2\mathrm{Ma} - \mathrm{Ma})$, where subtraction indicates the difference between simulations at the two different Mach numbers. Thus the convergence rate is estimated from a simulation at the value Ma in the left hand column, in conjunction with simulations at 2Ma and Ma/2.

Tables IV and VI show the expected second-order convergence towards the incompressible limit on a fixed grid as the Mach number tends to zero. The convergence at $t = 1.0$ on the 128^2 grid is rather poorer, as shown in Table V. This appears to be due to inadequate spatial resolution, as the dominant error is a diagonal grid-scale oscillation around thin current layers. Demonstrating convergence of the derivatives ω and j, instead of the primitive variables $\mathbf{u}$ and $\mathbf{B}$, is a particularly strenuous test in the presence of thin current layers.

The differences due to finite compressibility are fairly small compared with the spatial truncation errors. This is in line with the results of Dahlburg and Picone [22], who found that their $\mathrm{Ma} = 0.2$ solution was almost indistinguishable from their $\mathrm{Ma} = 0$ solution. Unfortunately at sufficiently large Mach numbers our algorithm was not stable enough to permit a direct comparison with the deviations at $\mathrm{Ma} = 0.4$ and $\mathrm{Ma} = 0.6$ found in [22], but it was just possible to discern weak jets emerging from the current layers. In any case, the

TABLE IV
Convergence with Mach Number: l_2 Errors at $t = 0.5$ on a 128×128 Grid

	Vorticity ω		Current j	
Mach number	l_2 error	Rate	l_2 error	Rate
0.277	2.89×10^{-2}		4.91×10^{-2}	
0.139	8.98×10^{-3}	1.68	1.55×10^{-3}	1.66
0.0693	1.92×10^{-3}	2.23	3.45×10^{-3}	2.17
0.0346	4.42×10^{-4}	2.11	8.56×10^{-4}	2.01
0.0173	1.08×10^{-4}	2.03	2.26×10^{-4}	1.93
0.0087	2.39×10^{-5}	2.17	3.87×10^{-5}	2.54

Note. The Mach numbers are of the form $\mathrm{Ma} = \sqrt{3}/n$. The errors are the l_2 difference between runs at Ma and Ma/2, and the convergence rates are computed from (symbolically) the l_2 differences $(\mathrm{Ma} - \mathrm{Ma}/2)/(2\mathrm{Ma} - \mathrm{Ma})$.

TABLE V
Convergence with Mach Number: l_2 Errors at $t = 1.0$ on a 128×128 Grid

	Vorticity ω		Current j	
Mach number	l_2 error	Rate	l_2 error	Rate
0.277	5.58×10^{-2}		8.35×10^{-2}	
0.139	1.31×10^{-2}	2.09	2.013×10^{-2}	2.05
0.0693	4.99×10^{-3}	1.39	8.63×10^{-3}	1.22
0.0346	1.25×10^{-3}	2.00	1.97×10^{-3}	2.13
0.0173	4.21×10^{-4}	1.57	7.71×10^{-4}	1.35
0.0087	1.63×10^{-4}	1.37	2.96×10^{-4}	1.38

Note. The Mach numbers are of the form $\mathrm{Ma} = \sqrt{3}/n$. The errors are the l_2 difference between runs at Ma and Ma/2, and the convergence rates are computed from (symbolically) the l_2 differences $(\mathrm{Ma} - \mathrm{Ma}/2)/(2\mathrm{Ma} - \mathrm{Ma})$.

unmodified nine-speed isothermal lattice Boltzmann equation becomes unstable at Mach numbers above about 0.2. Various thermal (varying θ) lattice Boltzmann schemes intended for compressible flows have been devised [1, 19] (see [17] for further references). Their stability at moderate Mach numbers has generally also been disappointing, although successful inviscid shock-tube simulations have been performed recently [75, 68]. In principle our lattice kinetic treatment of the magnetic field could be combined with one of these other hydrodynamic lattice Boltzmann schemes to simulate fully compressible MHD, but this topic requires further investigation.

9.2. Doubly Periodic Coalescence Instability

Many astrophysical processes seem to require a release of magnetic energy through resistive merging, or "reconnection," of magnetic field lines on timescales much shorter than a typical resistive diffusion time [4]. This involves the formation of thin current layers, across which magnetic field diffuses quickly. An equilibrium magnetic field comprising an array of magnetic islands, like that illustrated in Fig. 4, may be unstable to a coalescence

TABLE VI
Convergence with Mach Number: l_2 Errors at $t = 1.0$ on a 256×256 Grid

	Vorticity ω		Current j	
Mach number	l_2 error	Rate	l_2 error	Rate
0.277	5.53×10^{-2}		8.48×10^{-2}	
0.139	1.24×10^{-2}	2.16	2.01×10^{-2}	2.07
0.0693	4.79×10^{-3}	1.37	8.62×10^{-3}	1.22
0.0346	1.05×10^{-3}	2.19	1.76×10^{-3}	2.29
0.0173	2.42×10^{-4}	2.11	4.04×10^{-4}	2.12
0.0087	5.48×10^{-5}	2.14	9.46×10^{-5}	2.09

Note. The Mach numbers are of the form $\mathrm{Ma} = \sqrt{3}/n$. The errors are the l_2 difference between runs at Ma and Ma/2, and the convergence rates are computed from (symbolically) the l_2 differences $(\mathrm{Ma} - \mathrm{Ma}/2)/(2\mathrm{Ma} - \mathrm{Ma})$.

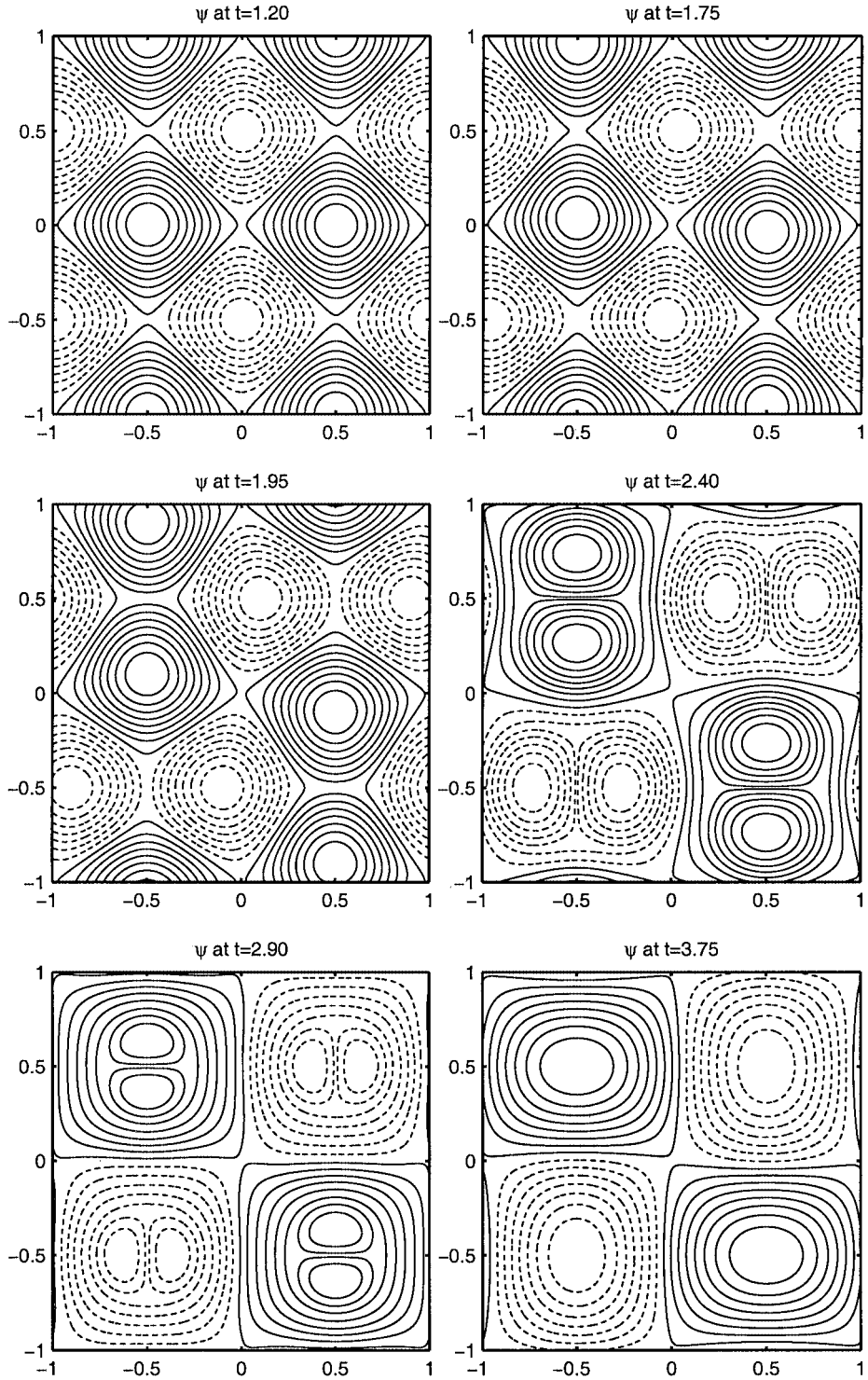

FIG. 4. Magnetic flux function $\psi(x, y)$ at times $t = 1.20$, 1.75, 1.95, 2.40, 2.90, and 3.40, for the doubly periodic coalescence instability with $\nu = 0.004$ and $\eta = 0.001$ and a 1024^2 grid. The nominal Mach number was $\sqrt{3}/40 \approx 0.0433$. Positive contours are solid lines; negative contours are dotted lines. This figure should be compared with Fig. 1 of [53].

instability [4, 50, 53]. In the initial stage, pairs of magnetic islands associated with currents of the same sign accelerate towards each other. This is an ideal MHD process which occurs on a fast inertial timescale. The pairs of islands subsequently merge on a slow diffusive timescale through the formation of thin current layers between colliding pairs of islands. For sufficiently low diffusivities the merging occurs on the diffusive Sweet–Parker [59, 70] timescale, i.e., at a rate proportional to $\eta^{1/2}$, via the formation of current layers with thickness $O(\eta^{-1/2})$ [4, 5, 50, 53].

Marliani and Strauss [53] recently investigated the coalescence instability developing from the initial conditions

$$\psi = \sin(\pi(x+y))\sin(\pi(x-y)), \quad \varphi = 10^{-4}\exp(-10(x^2+y^2)), \tag{64}$$

in the doubly periodic domain $-1 \le x, y \le 1$. This doubly periodic configuration, which had been used previously by Longcope and Strauss [50], is more convenient for numerical simulations than the configuration used by Biskamp and Welter [5], whose domain was periodic in one direction and nominally infinite in the other. Marliani and Strauss [53] used a second-order upwind scheme for the nonlinear terms, combined with a projection step to enforce $\nabla \cdot \mathbf{u} = \nabla \cdot \mathbf{B} = 0$. Their simulations were performed on a hierarchy of adaptively refined Cartesian grids, reaching an effective resolution of 8192^2 in the region of the current layers. For a fixed viscosity $\nu = 0.004$, and varying diffusivities $\eta = 0.008$, 0.004, 0.002, and 0.001, they verified the expected Sweet–Parker scaling, in which the reconnection rate is proportional to $\eta^{1/2}$.

We performed simulations for the same values of η and ν using our lattice kinetic scheme on various fixed grids with 256^2, 512^2, or 1024^2 points. The magnetic flux function at various times for the run with $\eta = 0.001$ and $\nu = 0.004$ is shown in Fig. 4, which should be compared with Fig. 1 of [53]. The time histories of the peak current for $\eta = 0.008$, 0.004, 0.002, and 0.001 are shown in Fig. 5, which should be compared with Fig. 2 of [53]. Most of our results compare favorably with those of Marliani and Strauss [53]. The magnetic flux function for the $\eta = 0.001$ and $\nu = 0.004$ simulation plotted in Fig. 4 is very similar to that in [53]. Any slight differences are most likely due either to the contour plotting or to the simulation not being completely resolved on our 1024^2 uniform grid. The high-frequency oscillations that are visible in the peak currents plotted in Fig. 5 are due to resolved acoustic modes, and they exactly coincided with runs at the same Mach number on different grids. They may be suppressed by choosing a Mach number smaller than the value of $\sqrt{3}/40 \approx 0.0433$ used, but at the price of taking proportionally more timesteps.

The most striking difference between the peak current histories plotted in Fig. 5, and those in Fig. 2 of Marliani and Strauss [53], is for the most resistive simulation, with $\eta = 0.008$ and $\nu = 0.004$. Our peak current $\max(|j|) \approx 67$ is much lower than the value $\max(|j|) \approx 200$ found in [53]. The instability also becomes visible significantly later, reaching its peak at around $t = 2.5$ instead of 2.0. At first sight this is surprising, because the most resistive simulation should also be the best resolved. However, we found exactly the same discrepancy using our spectral method, for 512^2 as well as 256^2 grids, and using initial data offset by half a lattice point. The linearly growing eigenmode, which has discontinous velocities in the ideal ($\nu = \eta = 0$) MHD case [51], was well resolved for $\eta = 0.008$, especially on the 512^2 grids. Finally, Fig. 6 shows that the peak current initially decays correctly as $\exp(-4\pi^2\eta t)$, since the unperturbed field ψ in (64) is an eigenfunction of the diffusion equation, before the instability became apparent.

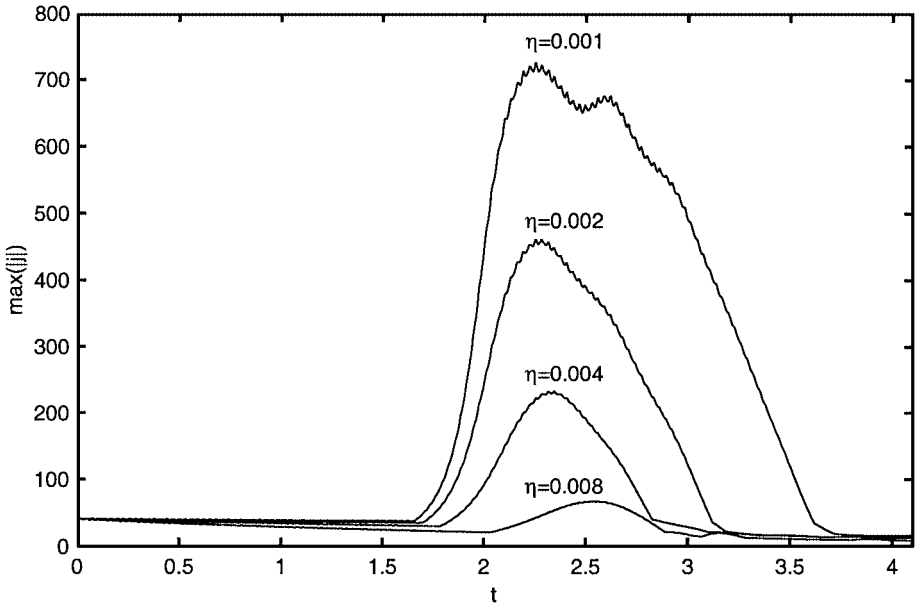

FIG. 5. Peak current as a function of time t in the doubly periodic coalescence instability with $\nu = 0.004$ and $\eta = 0.008$, 0.004, 0.002, and 0.001. The grids used were 256^2, 512^2, 1024^2, and 1024^2, respectively. This figure should be compared with Fig. 2 of [53]. The nominal Mach number was $\sqrt{3}/40 \approx 0.0433$. The high-frequency oscillations are due to resolved acoustic modes. They may be suppressed by using a smaller Mach number, but at the expense of requiring a larger number of timesteps.

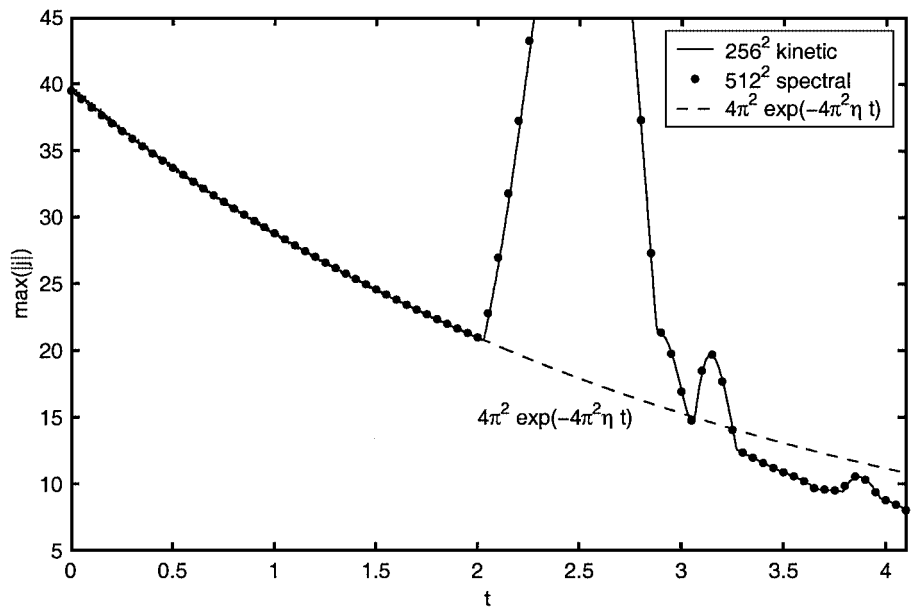

FIG. 6. Peak current as a function of time t in the doubly periodic coalescence instability with $\nu = 0.004$ and $\eta = 0.008$, the lowest line in Fig. 5 above. This figure should be compared with the lowest line in Fig. 2 of [53]. The almost coincident solid line (—) and dots (●) are the kinetic (256^2) and spectral (512^2) simulations, respectively. The dashed curve is the analytical result $\max(|j|) = 4\pi^2 \exp(-4\pi^2 \eta t)$ for the linear decay of the unperturbed magnetic islands. The nominal Mach number was $\sqrt{3}/80 \approx 0.0217$.

We believe this discrepancy is due to the timestep in [53] being too long to resolve resistive diffusion accurately. Marliani and Strauss's scheme was a modified form of the upwind projection method used by Bell *et al.* [2] for the incompressible Navier–Stokes equations, in which the diffusive terms were treated implicitly in combination with the projection onto divergence-free vector fields used to enforce incompressibility. The timestep in these schemes is usually based on a Courant condition of the form $\Delta t = O(\Delta x/u_{\max})$, for which an implicit treatment of diffusion is stable but often inaccurate. An accurate treatment of the diffusion would require a timestep $\Delta t = O(\Delta x^2/\eta)$, which is typically shorter. By contrast, the resistive and viscous diffusive terms in our spectral method were treated exactly using integrating factors, and the lattice kinetic scheme used short timesteps, $\Delta t = O(\mathrm{Ma}\Delta x/u_{\max})$, because the relevant Courant condition is based on the particle speeds rather than the macroscopic fluid speed. In fact, the oscillations in the peak current after its first maximum shown in [53] are systematically larger than in our simulations, which may also be due to an inaccurate treatment of diffusion in [53]. Politano *et al.* [61] and Lottermoser and Scholer [52] have found previously that Crank–Nicolson-like implicit treatments of the resistive diffusion term lead to inaccurate results when the timestep is set by an advective stability criterion. Minion and Brown [56] have also found an example in which automated adaptive mesh refinement on hierarchical Cartesian grids leads to *qualitatively* wrong results, namely the formation of spurious vortices in the 2D Navier–Stokes equations.

The most likely alternative explanation is that our own simulations were inadequately resolved, except that we found excellent agreement between the peak currents for different resolutions, and between the two completely different algorithms, as shown in Figs. 6 and 7 for the cases with $\eta = 0.008$ and 0.002, respectively. The excellent agreement may be partly

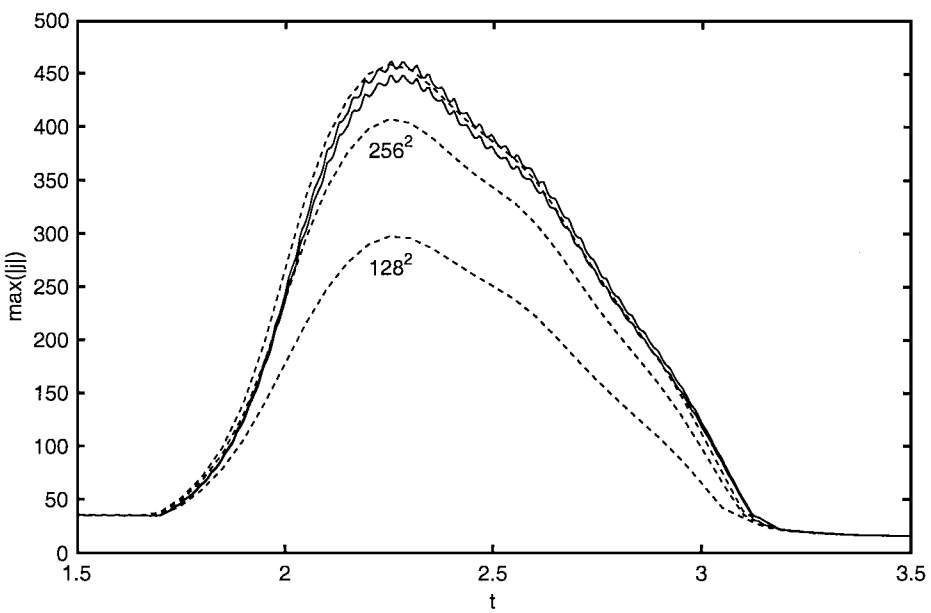

FIG. 7. Peak current as a function of time t in the doubly periodic coalescence instability with $\nu = 0.004$ and $\eta = 0.002$. The upper oscillatory solid line is the superimposed results from the 512^2 and 1024^2 lattice kinetic simulations, with nominal Mach number $\mathrm{Ma} = \sqrt{3}/40 \approx 0.0433$. The highest dotted line is the superimposed results from the 256^2 and 512^2 spectral simulations. The lower two dotted lines are from 128^2 and 256^2 spectral simulations, with initial conditions offset by half a lattice spacing. The lower solid line is from a 512^2 lattice kinetic simulation with initial conditions offset by half a lattice spacing.

because the symmetry of the initial conditions (64) ensures that the peak currents, in the middle of the current layers, form precisely at lattice points. To check this we performed some computations with initial data offset by half a lattice spacing, the lower two dotted lines in Fig. 7. The peak current histories for these computations also converge towards our previous results, even though the discrepancies for particular grids are considerably larger because the peak current formed halfway between lattice points. These discrepancies could probably be reduced by using an interpolation procedure to compute the peak current, instead of simply taking the maximum value achieved on the discrete lattice. We therefore believe that our results are correct, and that the treatment of resistivity by Marliani and Strauss [53] was inaccurate due to overlong timesteps.

10. CONCLUSION

We have devised a lattice kinetic scheme that simulates viscous and resistive incompressible magnetohydrodynamics. Simulations of two substantial problems, the Orszag–Tang vortex and the doubly periodic coalescence instability, compare favorably with previously published computations, and with reference solutions computed using a conventional spectral method. We have demonstrated the expected second-order convergence in Mach number, or timestep Δt, and in lattice spacing Δx. The scheme remained stable in the presence of thin current and vortex layers, which arise spontaneously in the 2D MHD equations.

As with conventional lattice Boltzmann schemes, our scheme is genuinely multidimensional and maintained a consistent approximation to $\nabla \cdot \mathbf{B} = 0$ to within machine round-off error. The algorithm generalises straightforwardly to three dimensions. Execution times on single processor workstations, shown in Table VII, are competitive with spectral methods in doubly periodic geometry. The much shorter cost per timestep of the lattice kinetic scheme is offset by the need to take $O(1/\mathrm{Ma})$ more timesteps. The lattice kinetic scheme should become very favorable when using multiple processors, because it is much easier to parallelise, or in nonperiodic geometries where the pressure equation would otherwise have to be solved iteratively.

The presented results were all computed on uniform grids. The extension to a hierarchy of adaptively refined Cartesian grids should be straightforward, using standard techniques for purely hyperbolic systems [48], and has been achieved for a hydrodynamic lattice Boltzmann scheme by Filippova and Hänel [28]. In fact, the extension is much simpler than

TABLE VII

CPU Time per Timestep for Spectral and Kinetic Methods on Various Grids

Resolution	Machine	Spectral timestep	Kinetic timestep	Ratio
512^2	Alpha (600-MHz 21164a)	3.70 s	0.322 s	0.087
512^2	SGI (300-MHz R12000)	3.20 s	0.383 s	0.119
512^2	Intel (1.6-GHz P4)	1.22 s	0.129 s	0.106
1024^2	Alpha	18.7 s	1.32 s	0.071
1024^2	SGI	20.8 s	1.57 s	0.075
1024^2	Intel	5.85 s	0.54 s	0.092
2048^2	Intel	33.8 s	2.42 s	0.072

Note. The lower cost per timestep of the kinetic method is offset by the need to take $O(1/\mathrm{Ma})$ more timesteps. The right hand column is thus effectively the breakeven Mach number. The kinetic method becomes more favorable for larger problems, presumably due partly to the extra $O(\log N)$ factor in the cost of the fast Fourier transforms.

for the upwind projection methods used by Marliani and coworkers [20, 33, 53], since there is no need to solve Poisson's equation on a hierarchy of grids. There is also scope for further work that implements boundary conditions other than periodic or homogeneous Dirichlet or Neumann via bounce-back, as in the Hartmann flow simulations.

Our scheme might best be thought of as part of a family of kinetic-based schemes for magnetohydrodynamics, one that includes conventional finite-volume discretisations using kinetic approximations for the fluxes [21, 41, 74]. For instance, the schemes of Xu [74] and Huba and Lyon [41] both used a velocity distribution function to compute upwind flux splittings, while retaining a macroscopic treatment of the magnetic field. Croisille *et al*. [21] used a kinetic treatment of the magnetic field leading to (10), which they then solved by a conventional finite-volume scheme. A discussion of kinetic finite-volume schemes for the compressible Euler equations with no magnetic field may be found in [31]. However, these approaches are restricted to simulating the ideal ($\eta = \nu = 0$) equations, whereas our scheme demonstrates the correct viscous and resistive behavior for finite values of ν and η. This extension of lattice Boltzman schemes using vector-valued distribution functions may prove useful for simulating other systems, such as polymeric liquids and other non-Newtonian fluids. In particular, since the current $\nabla \times \mathbf{B}$ is available at lattice points, a slightly modified scheme could be used to simulate generalised MHD equations, including the Hall effect or ambipolar diffusion. These generalised equations contain nonlinear or spatially varying second-derivative terms, so the integrating factor approach that makes spectral methods competitive for normal diffusion cannot be used.

APPENDIX: CALCULATION OF $\mathbf{\Lambda}^{(1)}$ AND $\mathbf{\Pi}^{(1)}$

The resistive term $\mathbf{\Lambda}^{(1)}$ in the electric field $\mathbf{\Lambda}$ is determined by Eq. (38),

$$\partial_{t_0} \mathbf{\Lambda}^{(0)}_{\alpha\beta} + \partial_\gamma \left(\sum_{i=0}^{M} \Xi_{i\gamma} \, \Xi_{i\alpha} \, g^{(0)}_{i\beta} \right) = -\frac{1}{\tau_m} \mathbf{\Lambda}^{(1)}_{\alpha\beta}. \tag{A.1}$$

We may compute $\partial_{t_0} \mathbf{\Lambda}^{(0)}_{\alpha\beta}$ using the known time derivatives $\partial_{t_0} u_\alpha$ and $\partial_{t_0} B_\alpha$ from the leading order momentum and induction equations,

$$\begin{aligned}
\partial_{t_0} \mathbf{\Lambda}^{(0)}_{\alpha\beta} &= \partial_{t_0} (u_\alpha B_\beta - u_\beta B_\alpha) \\
&= B_\beta \partial_{t_0} u_\alpha + u_\alpha \partial_{t_0} B_\beta - (\alpha \leftrightarrow \beta) \\
&= B_\beta (-\theta \partial_\alpha \log \rho - u_\gamma \partial_\gamma u_\alpha + \rho^{-1} \partial_\gamma M_{\gamma\alpha}) \\
&\quad - u_\alpha \partial_\gamma (u_\gamma B_\beta - u_\beta B_\gamma) - (\alpha \leftrightarrow \beta),
\end{aligned} \tag{A.2}$$

where $(\alpha \leftrightarrow \beta)$ denotes the previous terms with α and β interchanged, so that $\partial_{t_0} \mathbf{\Lambda}^{(0)}_{\alpha\beta} = -\partial_{t_0} \mathbf{\Lambda}^{(0)}_{\beta\alpha}$, and $M_{\gamma\alpha}$ is the Maxwell stress tensor from (27). The $O(u^2 B)$ and $O(u B^2)$ terms are both $O(\mathrm{Ma}^3)$ in our scalings, so (A.2) simplifies to

$$\mathbf{\Lambda}^{(1)}_{\alpha\beta} = -\tau_m [\Theta \partial_\alpha B_\beta - \theta B_\beta \partial_\alpha \log \rho + \theta B_\alpha \partial_\beta \log \rho + O(\mathrm{Ma}^3)]. \tag{A.3}$$

In nearly incompressible flow the density gradients $\nabla(\log \rho)$ are $O(\mathrm{Ma}^2)$, since we expect $\nabla p \sim c_s^2 \nabla \rho \sim \rho \mathbf{u} \cdot \nabla \mathbf{u}$. Thus the two terms involving $\mathbf{B}$ and $\log \rho$ are also $O(\mathrm{Ma}^3)$, leaving

$$\Lambda^{(1)}_{\alpha\beta} = -\tau_m \Theta [\partial_\alpha B_\beta + O(\mathrm{Ma}^3)]. \tag{A.4}$$

Similarly, the viscous stress $\mathbf{\Pi}^{(1)}$ is determined by Eq. (21),

$$\mathbf{\Pi}^{(1)} = -\tau\left[\partial_{t_0}\mathbf{\Pi}^{(1)} + \theta(\nabla(\rho\mathbf{u}) + \nabla(\rho\mathbf{u})^{\top} + \mathsf{I}\nabla\cdot(\rho\mathbf{u}))\right], \tag{A.5}$$

having evaluated $\sum_i \boldsymbol{\xi}_i\boldsymbol{\xi}_i\boldsymbol{\xi}_i f_i^{(0)}$ for the equilibria (23). We may compute $\partial_{t_0}\mathbf{\Pi}^{(0)}$ from known quantities,

$$\partial_{t_0}\mathbf{\Pi}^{(0)} = \partial_{t_0}(\theta\rho\,\mathsf{I} + \rho\mathbf{u}\mathbf{u}) = \mathsf{I}\theta\partial_{t_0}\rho + \mathbf{u}\partial_{t_0}(\rho\mathbf{u}) + \partial_{t_0}(\rho\mathbf{u}) - \mathbf{u}\mathbf{u}\partial_{t_0}\rho, \tag{A.6}$$

where $\partial_{t_0}\rho$ and $\partial_{t_0}(\rho\mathbf{u})$ are determined in Eq. (18). In the absence of a body force, this simplies to [25, 38, 64]

$$\mathbf{\Pi}^{(1)} = -\tau\theta\rho[\nabla\mathbf{u} + (\nabla\mathbf{u})^{\top}] + \tau\nabla\cdot(\rho\mathbf{u}\mathbf{u}\mathbf{u}), \tag{A.7}$$

which is a Newtonian viscous stress, plus an $O(\mathrm{Ma}^3)$ correction because the equilibria (23) are only accurate to $O(\mathbf{u}^2)$. If $\partial_{t_0}(\rho\mathbf{u})$ involves a body force $\mathbf{F}$ as well as the usual $\nabla\cdot(\rho\mathbf{u}\mathbf{u} + \theta\rho\,\mathsf{I})$ term, Eq. (A.7) acquires an extra term, $-\tau(\mathbf{F}\mathbf{u} + \mathbf{u}\mathbf{F})$ [23]. In continuum kinetic theory this term is canceled by higher moments of the continuum forcing term, leaving an unchanged viscous stress [23]. The changes made to $f_i^{(0)}$ in Section 4 to include a Maxwell stress, and possibly a uniform body force as in (61), leave $\sum_i \boldsymbol{\xi}_i\boldsymbol{\xi}_i\boldsymbol{\xi}_i f_i^{(0)}$ unchanged, but the mere presence of a body force like $\mathbf{F} = \mathbf{J}\times\mathbf{B}$ in the macroscopic momentum equation for $\partial_{t_0}(\rho\mathbf{u})$ is enough to change the viscous stress by $-\tau(\mathbf{F}\mathbf{u} + \mathbf{u}\mathbf{F})$, as indicated.

ACKNOWLEDGMENTS

Financial support from St. John's College, Cambridge, UK, is gratefully acknowledged. The numerical experiments made use of the portable fast Fourier transform library FFTW by Frigo and Johnson [29].

REFERENCES

1. F. J. Alexander, J. D. Sterling, and S. Chen, Lattice Boltzmann thermohydrodynamics, *Phys. Rev. E* **47**, R2249 (1993), doi:10.1103/PhysRevE.47.R2249.
2. J. B. Bell, P. Colella, and H. M. Glaz, A second-order projection method for the incompressible Navier–Stokes equations, *J. Comput. Phys.* **85**, 257 (1989).
3. P. L. Bhatnagar, E. P. Gross, and M. Krook, A model for collision process in gases. I. Small amplitude processes in charged and neutral one-component system, *Phys. Rev.* **94**, 511 (1954), doi:10.1103/PhysRevE.94.511.
4. D. Biskamp, *Nonlinear Magnetohydrodynamics* (Cambridge University Press, Cambridge, UK, 1993).
5. D. Biskamp and H. Welter, Coalescence of magnetic islands, *Phys. Rev. Lett.* **44**, 1069 (1980).
6. D. Biskamp and H. Welter, Dynamics of decaying two-dimensional magnetohydrodynamic turbulence, *Phys. Fluids B* **1**, 1964 (1989), doi:10.1063/1.859060.
7. F. Bouchut, Construction of BGK models with a family of kinetic entropies for a given system of conservation laws, *J. Stat. Phys.* **95**, 113 (1999).
8. J. P. Boyd, *Chebyshev and Fourier Spectral Methods* (Dover, New York, 2000), 2nd ed.
9. M. Brio and C. C. Wu, An upwind differencing scheme for the equations of ideal magnetohydrodynamics, *J. Comput. Phys.* **75**, 400 (1988).
10. C. Canuto, M. Y. Hussaini, A. Quarteroni, and T. A. Zang, *Spectral Methods for Fluid Dynamics* (Springer-Verlag, New York, 1988).
11. C. Cercignani, *The Boltzmann Equations and its Applications* (Springer-Verlag, New York, 1988).

12. S. Chapman and T. G. Cowling, *The Mathematical Theory of Non-Uniform Gases* (Cambridge University Press, Cambridge, UK, 1991), 3rd ed.
13. G. Q. Chen, C. D. Levermore, and T. P. Liu, Hyperbolic conservation-laws with stiff relaxation terms and entropy, *Commun. Pure Appl. Math.* **47**, 787 (1994).
14. H. Chen, S. Chen, and W. H. Matthaeus, Recovery of the Navier–Stokes equations using lattice-gas Boltzmann method, *Phys. Rev. A* **45**, R5339 (1992), doi:10.1103/PhysRevA.45.R5339.
15. H. Chen, W. H. Matthaeus, and L. W. Klein, An analytic theory and formulation of a local magnetohydrodynamic lattice gas model, *Phys. Fluids* **31**, 1439 (1988), doi:10.1063/1.866735.
16. S. Chen, H. Chen, D. O. Martínez, and W. H. Matthaeus, Lattice Boltzmann model for simulation of magnetohydrodynamics, *Phys. Rev. Lett.* **67**, 3776 (1991), doi:10.1103/PhysRevLett.67.3776.
17. S. Chen and G. D. Doolen, Lattice Boltzmann method for fluid flows, *Annu. Rev. Fluid Mech.* **30**, 329 (1998).
18. S. Chen, D. O. Martínez, W. H. Matthaeus, and H. D. Chen, Magnetohydrodynamics computations with lattice gas automata, *J. Stat. Phys.* **68**, 533 (1992).
19. Y. Chen, H. Ohashi, and M. Akiyama, Thermal lattice Bhatnagar-Gross-Krook model without nonlinear deviations in macrodynamic equations, *Phys. Rev. E* **50**, 2776 (1994), doi:10.1103/PhysRevE.50.2776.
20. D. Cordoba and C. Marliani, Evolution of current sheets and regularity of ideal incompressible magnetic fluids in 2D, *Commun. Pure Appl. Math.* **53**, 512 (2000).
21. J.-P. Croisille, R. Khanfir, and G. Chanteur, Numerical simulation of the MHD equations by a kinetic-type method, *J. Sci. Comput.* **10**, 81 (1995).
22. R. B. Dahlburg and J. M. Picone, Evolution of the Orszag–Tang vortex system in a compressible medium. I. Initial average subsonic flow, *Phys. Fluids B* **1**, 2153 (1989), doi:10.1063/1.859081.
23. P. J. Dellar, Non-hydrodynamic modes and *a priori* construction of shallow water lattice Boltzmann equations, *Phys. Rev. E* **65**, 036309 (2002), doi:10.1103/PhysRevE.65.036309.
24. P. J. Dellar, *A priori* derivation of lattice Boltzmann equations for rotating fluids, submitted for publication.
25. P. J. Dellar, Bulk and shear viscosities in lattice Boltzmann equations, *Phys. Rev. E* **64**, 031203 (2001), doi:10.1103/PhysRevE.64.031203.
26. P. J. Dellar, A note on magnetic monopoles and the one dimensional MHD Riemann problem, *J. Comput. Phys.* **172**, 392 (2001), doi:10.1006/jcph.2001.6815.
27. G. Einaudi and M. Velli, The distribution of flares, statistics of magnetohydrodynamic turbulence and coronal heating, *Phys. Plasmas* **6**, 4146 (1999), doi:10.1063/1.873679.
28. O. Filippova and D. Hänel, Grid refinement for lattice-BGK models, *J. Comput. Phys.* **147**, 219 (1998), doi:10.1006/jcph.1998.6089.
29. M. Frigo and S. G. Johnson, FFTW: An adaptive software architecture for the FFT, in *Proceedings of the IEEE International Conference on Acoustics, Speech, and Signal Processing, Seattle, 1998* (IEEE Press, Piscataway, NJ, 1998), Vol. 3, p. 1381, available at http://www.fftw.org/.
30. U. Frisch, B. Hasslacher, and Y. Pomeau, Lattice-gas automata for the Navier–Stokes equations, *Phys. Rev. Lett.* **56**, 1505 (1986), doi:10.1103/PhysRevLett.56.1505.
31. E. Godlewski and P.-A. Raviart, *Numerical Approximation of Hyperbolic Systems of Conservation Laws* (Springer-Verlag, New York, 1996).
32. H. Grad, Principles of the kinetic theory of gases, in *Thermodynamik der Gase*, edited by S. Flügge, *Handbuch der Physik* (Springer-Verlag, Berlin, 1958), Vol. 12, p. 205.
33. R. Grauer and C. Marliani, Geometry of singular structures in magnetohydrodynamic flows, *Phys. Plasmas* **5**, 2544 (1998), doi:10.1063/1.872939.
34. X. He, S. Chen, and G. D. Doolen, A novel thermal model of the lattice Boltzmann method in incompressible limit, *J. Comput. Phys.* **146**, 282 (1998), doi:10.1006/jcph.1998.6057.
35. X. He and L.-S. Luo, *A priori* derivation of the lattice Boltzmann equation, *Phys. Rev. E* **55**, R6333 (1997), doi:10.1103/PhysRevE.55.R6333.
36. X. He and L.-S. Luo, Theory of the lattice Boltzmann method: From the Boltzmann equation to the lattice Boltzmann equation, *Phys. Rev. E* **56**, 6811 (1997), doi:10.1103/PhysRevE.56.6811.

37. X. He, X. Shan, and G. D. Doolen, Discrete Boltzmann equation model for nonideal gases, *Phys. Rev. E* **57**, R13 (1998), doi:10.1103/PhysRevE.57.R13.
38. S. Hou, Q. Zou, S. Chen, G. D. Doolen, and A. C. Cogley, Simulation of cavity flow by the lattice Boltzmann equation, *J. Comput. Phys.* **118**, 329 (1995), doi:10.1006/jcph.1995.1103.
39. T. Y. Hou, J. S. Lowengrub, and M. J. Shelley, Removing the stiffness from interfacial flow with surface-tension, *J. Comput. Phys.* **114**, 312 (1994), doi:10.1006/jcph.1994.1170.
40. K. Huang, *Statistical Mechanics* (Wiley, New York, 1987), 2nd ed.
41. J. D. Huba and J. G. Lyon, A new 3D MHD algorithm: The distribution function method, *J. Plasma Phys.* **61**, 391 (1999).
42. P. Janhunen, A positive conservative method for magnetohydrodynamics based on HLL and Roe methods, *J. Comput. Phys.* **160**, 649 (2000), doi:10.1006/jcph.2000.6479.
43. A. Jeffrey and T. Taniuti, *Nonlinear Wave Propagation* (Academic, New York, 1964).
44. S. Jin and Z. P. Xin, The relaxation schemes for systems of conservation laws in arbitrary space dimensions, *Commun. Pure Appl. Math.* **48**, 235 (1995).
45. L. D. Landau and E. M. Lifshitz, *Fluid Mechanics* (Pergamon, Oxford, 1987), 2nd ed.
46. R. J. LeVeque, *Numerical Methods for Conservation Laws* (Birkhäuser, Basel, 1992), 2nd ed.
47. R. J. LeVeque, Wave propagation algorithms for multidimensional hyperbolic systems. *J. Comput. Phys.* **131**, 327 (1997), doi:10.1006/jcph.1996.5603.
48. R. J. LeVeque, Nonlinear conservation laws and finite volume methods for astrophysical fluid flow, in *Computational Methods for Astrophysical Fluid Flow*, edited by O. Steiner and A. Gautschy, 27th Saas-Fee Advanced Course Lecture Notes (Springer-Verlag, New York, 1998), p. 1.
49. R. J. LeVeque and M. Pelanti, A class of approximate Riemann solvers and their relation to relaxation schemes, *J. Comput. Phys.* **172**, 572 (2001), doi:10.1006/jcph.2001.6838.
50. D. W. Longcope and H. R. Strauss, The coalescence instability and the development of current sheets in two-dimensional magnetohydrodynamics, *Phys. Fluids B* **5**, 2858 (1993), doi:10.1063/1.860673.
51. D. W. Longcope and H. R. Strauss, Spontaneous reconnection of line-tied flux tubes, *Astrophys. J.* **426**, 742 (1994).
52. R. F. Lottermoser and M. Scholer, Undriven magnetic reconnection in magnetohydrodynamics and Hall magnetohydrodynamics, *J. Geophys. Res. A* **102**, 4875 (1997).
53. C. Marliani and H. R. Strauss, Reconnection of coalescing magnetic islands, *Phys. Plasmas* **6**, 495 (1999), doi:10.1063/1.873193.
54. D. O. Martínez, S. Chen, and W. H. Matthaeus, Lattice Boltzmann magnetohydrodynamics, *Phys. Plasmas* **1**, 1850 (1994), doi:10.1063/1.870640.
55. G. R. McNamara and G. Zanetti, Use of the Boltzmann equation to simulate lattice-gas automata, *Phys. Rev. Lett.* **61**, 2332 (1988). doi:10.1103/PhysRevLett.61.2332.
56. M. L. Minion and D. L. Brown, Performance of under-resolved two-dimensional incompressible flow simulations, II, *J. Comput. Phys.* **138**, 734 (1997), doi:10.1006/jcph.1997.5843.
57. D. Montgomery and G. D. Doolen, Magnetohydrodynamic cellular automata, *Phys. Lett. A* **120**, 229 (1987).
58. S. A. Orszag and C.-M. Tang, Small-scale structure of two-dimensional magnetohydrodynamic turbulence, *J. Fluid Mech.* **90**, 129 (1979).
59. E. N. Parker, The solar flare phenomenon and the theory of reconnection and annihilation of magnetic fields, *Astrophys. J. Suppl.* **8**, 177 (1963).
60. J. M. Picone and R. B. Dahlburg, Evolution of the Orszag–Tang vortex system in a compressible medium. II. Supersonic flow, *Phys. Fluids B* **3**, 29 (1991), doi:10.1063/1.859953.
61. H. Politano, A. Pouquet, and P. L. Sulem, Inertial ranges and resistive instabilities in two-dimensional magnetohydrodynamic turbulence, *Phys. Fluids B* **1**, 2330 (1989), doi:10.1063/1.859051.
62. A. Pouquet, P. L. Sulem, and M. Meneguzzi, Influence of velocity-magnetic field correlations on decaying magnetohydrodynamic turbulence with neutral X points, *Phys. Fluids* **31**, 2635 (1988), doi:10.1063/1.866541.

63. K. G. Powell, *An Approximate Riemann Solver for Magnetohydrodynamics (That Works in More Than One Dimension)*, ICASE Report 94-24 (Institute for Computer Applications in Science and Engineering, NASA Langley Research Center, 1994), available at http://www.icase.edu/library/reports/rdp/1994.html#94–24.

64. Y.-H. Qian and S. A. Orszag, Lattice BGK models for the Navier–Stokes equation—nonlinear deviation in compressible regimes, *Europhys. Lett.* **21**, 255 (1993).

65. Y.-H. Qian and Y. Zhou, Complete Galilean-invariant lattice BGK models for the Navier–Stokes equation, *Europhys. Lett.* **42**, 359 (1998); also `ICASE Report TR-98-38` (Institute for Computer Applications in Science and Engineering, NASA Langley Research Center, 1998).

66. X. Shan and X. He, Discretization of the velocity space in the solution of the Boltzmann equation, *Phys. Rev. Lett.* **80**, 65 (1998), doi:10.1103/PhysRevLett.80.65.

67. J. A. Shercliff, *A Textbook of Magnetohydrodynamics* (Pergamon, Oxford, 1965).

68. W. P. Shi, W. Shyy, and R. W. Mei, Finite-difference-based lattice Boltzmann method for inviscid compressible flows, *Numer. Heat Transfer B* **40**, 1 (2001).

69. S. Succi, M. Vergassola, and R. Benzi, Lattice Boltzmann scheme for two-dimensional magnetohydrodynamics, *Phys. Rev. A* **43**, 4521 (1991), doi:10.1103/PhysRevA.43.4521.

70. P. A. Sweet, The production of high energy particles in solar flares, *Nuovo Cimento Suppl.* **8**, 188 (1958).

71. G. Tóth, The $\nabla \cdot \mathbf{B} = 0$ constraint in shock-capturing magnetohydrodynamics codes, *J. Comput. Phys.* **161**, 605 (2000), doi:10.1006/jcph.2000.6519.

72. J. R. Weimar and J. P. Boon, Nonlinear reactions advected by a flow, *Physica A* **224**, 207 (1996).

73. P. R. Woodward and W. Dai, An approximate Riemann solver for ideal magnetohydrodynamics, *J. Comput. Phys.* **111**, 354 (1994), doi:10.1006/jcph.1994.1069.

74. K. Xu, Gas-kinetic theory-based flux splitting method for ideal magnetohydrodynamics, *J. Comput. Phys.* **153**, 334 (1999), doi:10.1006/jcph.1999.6280.

75. G. W. Yan, Y. S. Chen, and S. X. Hu, Simple lattice Boltzmann model for simulating flows with shock wave, *Phys. Rev. E* **59**, 454 (1999).